Article

Measurements and Modelling of Vapour–Liquid Equilibrium for (H_2O + N_2) and (CO_2 + H_2O + N_2) Systems at Temperatures between 323 and 473 K and Pressures up to 20 MPa

Yolanda Sanchez-Vicente [1,2,*] and J. P. Martin Trusler [1]

[1] Qatar Carbonates and Carbon Storage Research Centre (QCCSRC), Department of Chemical Engineering, Imperial College London, South Kensington Campus, London SW7 2AZ, UK; m.trusler@imperial.ac.uk
[2] Department of Mechanical & Construction Engineering, Faculty of Engineering and Environment, Northumbria University, Newcastle upon Tyne NE1 8ST, UK
[*] Correspondence: yolanda.vicente@northumbria.ac.uk

Abstract: Understanding the phase behaviour of (CO_2 + water + permanent gas) systems is critical for implementing carbon capture and storage (CCS) processes, a key technology in reducing CO_2 emissions. In this paper, phase behaviour data for (H_2O + N_2) and (CO_2 + H_2O + N_2) systems are reported at temperatures from 323 to 473 K and pressures up to 20 MPa. In the ternary system, the mole ratio between CO_2 and N_2 was 1. Experiments were conducted in a newly designed analytical apparatus that includes two syringe pumps for fluid injection, a high-pressure equilibrium vessel, heater aluminium jacket, Rolsi sampling valves and an online gas chromatograph (GC) for composition determination. A high-sensitivity pulsed discharge detector installed in the GC was used to measure the low levels of dissolved nitrogen in the aqueous phase and low water levels in the vapour phase. The experimental data were compared with the calculation based on the γ-φ and SAFT-γ Mie approaches. In the SAFT-γ Mie model, the like parameters for N_2 had to be determined. We also obtained the unlike dispersion energy for the (H_2O + N_2) system and the unlike repulsive exponent and dispersion energy for the (CO_2 + N_2) system. This was done to improve the prediction of SAFT-γ Mie model. For the (H_2O + N_2) binary system, the results show that the solubility of nitrogen in the aqueous phase was calculated better by the γ-φ approach rather than the SAFT-γ Mie model, whereas SAFT-γ Mie performed better for the prediction of the vapour phase. For the (CO_2 + H_2O + N_2) ternary systems, both models predicted the experimental data for each phase with good agreement.

Keywords: carbon dioxide; water; nitrogen; carbon capture and storage; vapour–liquid equilibrium; high pressure; high temperature; SAFT-γ Mie; NRTL model

1. Introduction

The IPCC Special Report on "Global Warming of 1.5 °C" stressed the urgency of achieving net-zero emissions by mid-century to mitigate the worst predicted climate change consequences [1]. At COP26 in Glasgow, commitments to net-zero emissions were made, covering 90% of global GDP and around 90% of global emissions. This goal can probably only be achieved by implementing carbon capture and storage (CCS) in particular sectors, such as power and industry, as a part of the overall decarbonisation strategy. Investing in CCS can also benefit low-carbon hydrogen production from natural gas [2]. Furthermore, CCS provides a framework for reducing carbon dioxide levels in the atmosphere in combination with bioenergy and/or direct air capture [3].

CCS is usually described as a chain of three processes. In the first step, CO_2 emissions from large-scale industrial or power-production processes are captured or avoided by various techniques, including post-combustion scrubbing, pre-combustion reforming, chemical looping and oxyfuel combustion. Next, the CO_2 stream is compressed and transported by

means of pipeline or ship and, in the final step, injected into a geological storage reservoir. Potential sinks for CO_2 include active and depleted hydrocarbon reservoirs, unminable coal seams and deep saline aquifers. The CO_2 stream exported from the capture plant may contain many impurities, including N_2, H_2, O_2, Ar, H_2S, SO_2, NO_x, CO, CH_4 and H_2O [4]. The type and quantity of the impurity in the CO_2 stream would be controlled by the purity levels agreed to and managed by the transport and storage operators [5].

The thermophysical properties of CO_2 and its mixtures with impurities and reservoir fluids (brines and hydrocarbons) considerably impact the design and operation of the transportation process and the storage processes. For instance, knowledge of the phase behaviour of impure CO_2 is essential to prevent phase separation in the pipeline [6,7]. Another example is that the CO_2 storage capacity of a saline aquifer depends on the phase behaviour, saturated phase densities and interfacial properties of the (CO_2 + impurities + brine) system under reservoir conditions [8,9]. Furthermore, thermophysical data for CO_2-rich mixtures, including phase equilibrium data, are needed to develop thermodynamic models, such as equations of state required for the process design and simulation [10].

Both carbon storage in saline aquifers and CO_2 transportation processes require knowledge of the vapour–liquid equilibrium of (CO_2 + H_2O + N_2) mixtures. The phase behaviour of (H_2O + N_2) binary systems have been reported extensively in the literature. Table 1 lists the published data, including the phases analysed and the pressure and temperature ranges. According to the IUPAC assessment of solubility data for nitrogen in water [11], the data of Smith and colleagues [12,13] and Wiebe et al. [14,15] are recommended for the temperature range of 298.15 K to 398.15 K. For water solubility in nitrogen, close agreement exists between the data of Folas et al. [16], Mohammadi et al. [17], Rigby and Prausnitz [18] and Maslennikova et al. [19]. Thus, these can be considered reliable data sources. The much more extensive vapour–liquid equilibrium data available for (CO_2 + H_2O) binary systems were reviewed by Spycher et al. [20,21], Diamond and Akinfiev [22] and Chapoy et al. [23]. On the other hand, experimental data for the (CO_2 + H_2O + N_2) ternary system are scarce in the literature, and the few available sources are detailed Table 2. These cover a narrow temperature range from 273 K to 318 K. Therefore, more ternary data are required to test the predictive capability of the thermodynamic models.

Table 1. Literature data of the (H_2O + N_2) binary system.

Reference	Year	Type	T_{min}/K	T_{max}/K	p_{min}/MPa	p_{max}/MPa
Goodman and Krase [24]	1931	*Tpx*	273	442	10.1	30.4
Wiebe et al. [14]	1932	*Tpx*	298	298	2.5	101.3
Wiebe et al. [15]	1933	*Tpx*	298	373	2.5	101.3
Saddington and Krase [25]	1934	*Tpxy*	323	513	10.1	30.4
Sidorov et al. [26]	1953	*Tpy*	373	373	5.1	40.5
Bukacek [27]	1955	*Tpy*	378	378	7.0	68.3
Smith et al. [12]	1962	*Tpx*	303	303	1.1	5.9
O'Sullivan et al. [13]	1966	*Tpx*	325	325	10.1	60.8
Rigby and Prausnitz [18]	1968	*Tpy*	298	373	2.1	10.2
Maslennikova [28]	1971	*Tpy*	473	613	10.5	46.1
Maslennikova et al. [19]	1971	*Tpy*	298	623	5.1	50.7
Kosyakov et al. [29]	1977	*Tpy*	233	273	1.0	10.1
Brunner [30]	1978	*Tpy*	513	513	10.1	20.2
Gillespie and Wilson [31]	1980	*Tpxy*	311	478	0.3	13.8
Japas and Franck [32]	1985	*Tpxy*	580	638	21.0	270.5
Li and Nghiem [33]	1986	*Tpx*	324	398	10.4	10.4
Alvarez and Fernandez-Prini [34]	1991	*Tpx*	583	613	17.2	54.4
Fenghour et al. [35]	1993	*Tpx*	410	595	7.8	23.5
Ugrozov [36]	1996	*Tpy*	311	366	0.3	13.8
Blanco et al. [37]	1999	*Tpy*	253	283	0.4	9.9

Table 1. *Cont.*

Reference	Year	Type	T_{min}/K	T_{max}/K	p_{min}/MPa	p_{max}/MPa
Blanco et al. [38]	2002	*Tpy*	263	283	0.5	10.0
Chapoy et al. [39]	2004	*Tpx*	274	363	1.0	7.0
Mohammadi et al. [17]	2005	*Tpy*	283	363	0.4	5.0
Folas et al. [16]	2007	*Tpy*	258	293	0.5	20.0
Tabasinejad et al. [40]	2011	*Tpy*	422	483	3.8	133.7
Liu et al. [41]	2012	*Tpx*	308	318	8.0	16.0
Muromachi et al. [42]	2017	*Tpx*	292	307	3.0	7.0

Table 2. Literature phase behaviour data of (CO_2 + H_2O + N_2) ternary system.

Reference	Year	Type	T_{min}/K	T_{max}/K	P_{min}/MPa	P_{max}/MPa
Zelvenskii [43]	1939	*Tpx*	298	298	2.5	29.4
Liu et al. [41]	2012	*Tpxy*	308	318	8.0	16.0
Foltran et al. [44]	2015	*Tpy*	313	313	8.9	17.2
Hassanpouryouzband et al. [45]	2019	*Tpxy*	273	303	1.5	20.8

Various models have been proposed to describe the phase behaviour of mixtures such as (CO_2 + H_2O) or (H_2O + N_2) [10,23]. One of the most popular is the γ-φ approach, in which an activity coefficient model coupled with Henry's law describes the liquid phase, and an equation of state, such as the Peng–Robinson equation (PR-EOS), describes the vapour phase [6]. Using this approach, several researchers were able to accurately describe vapour–liquid equilibria for (CO_2 + H_2O) and (H_2O + N_2) [17,18,46,47]. In certain cases, the vapour–liquid equilibria of these mixtures have been correlated by the φ-φ approach, in which an equation of state is used for both phases. Chapoy et al. used the φ-φ approach, adjusting the binary interaction parameter to fit the solubility of N_2 in water, and they found that the predictions were reasonably accurate [39].

Cubic equations of state (cEoS) are built on the assumption that the molecules are rigid spheres that interact by van der Waals forces. However, because water and carbon dioxide deviate considerably from these concepts, it is expected that cEoS are not very good at predicting their phase behaviour. As a result, more sophisticated state equations that account for a broader range of interactions have been applied to this type of system. The cubic-plus-association equation state (CPA EoS), which incorporates an association term, has been applied successfully to (H_2O + N_2) and (H_2O + CO_2) systems [16,40,42,48]. Furthermore, molecular-based models, such as the statistical associating fluid theory (SAFT), that can account for van der Waals, polar and hydrogen-bonding interactions have been successfully applied recently in the description of (CO_2 + H_2O) systems [49,50]. Another model used to describe binary and multi-component mixtures specific to CCS processes is the GERG-2008 EoS, a well-known empirical multi-fluid Helmholtz energy model. However, the original version of this model presents certain limitations for CCS processes because it was created to determine the thermodynamic properties of natural gas and similar mixtures of as many as 21 components [51]. To address these limitations for the CO_2-rich mixtures commonly used in CCS processes, Gernert and Span [52] developed the EOS-CG mixture model. EOS-CG has been shown to accurately describe the phase behaviour of (CO_2 + H_2O) and (N_2 + H_2O) systems [53].

In this paper, we report new phase behaviour data of (H_2O + N_2) and (CO_2 + H_2O + N_2) systems at temperatures ranging from 323 K to 473 K and at pressures up to 20 MPa. These data are needed for both CO_2 transportation and carbon storage processes. In the literature, high-pressure phase equilibria for binary system have been reported. However, data for the ternary mixture have never been published at temperatures above 318 K. Experiments were conducted in a bespoke analytical apparatus. The experimental results were compared to the calculations based on the γ-φ and SAFT-γ Mie approaches. These models are widely used to model the phase behaviour of H_2O + gas systems.

2. Materials and Methods

2.1. Materials

Pure deionised water with an electrical resistivity > 18 MΩ·cm at T = 298 K was used (produced by a Millipore water purification unit). Prior to the experiments, the water was degassed under vacuum with stirring. Table 3 presents details of the gases used in this work; each was used as received.

Table 3. Description of chemicals, where x denotes mole fraction, and ρ_{elec} denotes electrical resistivity at T = 298 K.

Chemical Name	CAS Number	Source	Purity as Supplied	Additional Purification
H_2O	7732-18-5	Millipore Direct Q UV3	ρ_{elec} >18 MΩ·cm	degassed under vacuum
CO_2	124-38-9	BOC	$x \geq 0.99995$	none
N_2	108-87-2	BOC	$x \geq 0.99998$	none
$0.5\,CO_2 + 0.5\,N_2$		BOC	$x \geq 0.99995$	none

2.2. Apparatus

An analytical apparatus developed in our laboratory and described previously [46] was modified for this project. The modified analytical apparatus includes three syringe pumps for fluid injection, a high-pressure equilibrium cell, an aluminium heater jacket and sampling valves coupled to an online gas chromatograph (GC) for composition measurements. The GC was fitted with a pulse discharge helium ionisation detector (PDHID) and a thermal conductivity detector (TCD). Figure 1 shows the key components of the apparatus.
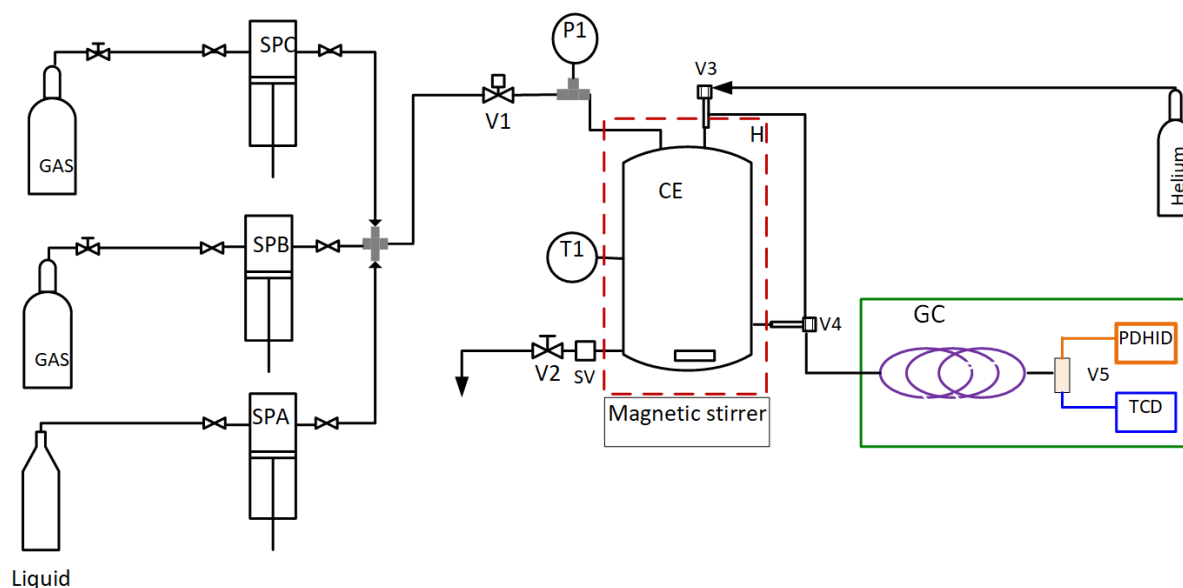
Figure 1. Schematic of the analytic-phase equilibrium apparatus: SPA, SPB and SPC syringe pumps. V1, a pneumatically operated valve; V2, needle valve; V3 and V4, Rolsi sampling valves; SV, rupture-disc pressure relief; CE, equilibrium cell; H, aluminium heat jacket; T1, temperature sensor; P1 pressure transducer; GC, gas chromatograph; V5, Deans Switching valve; thermal conductivity detector (TCD) and pulse-discharge helium ionization detector (PDHID).

The equilibrium vessel was based on the design previously described by Fandiño et al. [54]. The vessel, made from stainless steel A-286 (EN 1.4980), consisted of a blind cylinder with an internal volume of 77 cm^3, a seal-retaining ring and a flat-plate closure retained by six bolts. The vessel was sealed by a silver-plated hollow stainless-steel O ring internally pressurised with nitrogen (Wills Ring, type MOT, Trelleborg, Gloucestershire, UK). Two fluid ports were bored though the side of the main body and used for the fluid outlet and

liquid sampling. Two further fluid ports were bored though the lid and used for fluid inlet and vapour sampling. The new cell was designed for temperatures up to 473 K and pressures up to 40 MPa. A rupture-disk safety device was installed in the fluid outlet line to protect against unintended over pressurisation. To control the temperature, the cell was enclosed in an aluminium thermostatic jacket equipped with four electric cartridge heaters (Firerod, Watlow Co., UK), a platinum resistance thermometer (514-183, TC Ltd., UK) and a PID controller (Eurotherm 2216e, Schneider Electric SE, UK). A silicone–rubber sponge sheet was wrapped around the thermostatic jacket to insulate the cell. The cell temperature was measured by a platinum resistance thermometer (PT100, Sensing Devices Ltd., Southport, UK) inserted into a blind axial hole drilled into the wall of the pressure vessel. The pressure was measured by a pressure transducer (Honeywell, Super TJE model, UK) located in the outlet tube from the cell. The thermometer and the pressure transducer were connected to a data acquisition/switch unit (Agilent Technologies, model 34970A, UK) that measured the resistance of the former and the voltage generated by the latter and communicated the data to a control computer.

To mix the fluids, the vessel contained a PTFE-coated magnetic stirrer bar, and the apparatus was placed on top of a magnetic stirrer plate (UC151, Stuart Equipment, Fisher Scientific, UK). A pneumatically operated valve (model CV-420, Vindum Engineering, Sandpoint, USA) was mounted in the inlet line and used to isolate the vessel from the pumps during equilibration. Injection of the fluids was accomplished by three syringe pumps (Quizix pump, Q5310-HC-A-GH-S model, Vindum Engineering, Sandpoint, United States) attached to the inlet port of the cell in parallel.

Two electromagnetic sampling valves (ROLSI Evolution IV,), each connected to the cell via a capillary tube (0.13 mm ID × 1.6 mm OD × 80 mm length), were used to withdraw small samples of the liquid and vapour phases without disrupting the equilibrium. A heated transfer line with helium flow connected the two ROLSI valves in series with the GC. The ROLSI valves and the transfer line were maintained at T = 473 K, assuring fast vaporisation of the sample. The GC (Agilent 7890A, UK) was provided with a split/spitless injector, HP-PLOT-Q capillary column (0.32 mm OD × 30 m length, film thickness 20 μm) and two detectors: a pulse-discharge helium ionisation detector (PDHID) and a thermal conductivity detector (TCD). The PDHID detector (D-3-I-HP, Vici) was selected because of its high sensitivity, commonly used at the ppm and ppb levels [55]. This detector permitted us to quantify low levels of gas dissolved in the aqueous phase and low levels of water vapour in the gas phase. A Deans switching system (DSS, Agilent, UK) was installed to select the detector to be used. In this way, the detector could be selected according to the concentration level of the compound in the sample. A program written in Keysight VEE was developed to control the operation of the sampling valves, activate the GC and log the temperature and pressure, thereby permitting complete automation of data collection. Standard uncertainties of pressure and temperature were 0.01 MPa and 0.02 K, respectively.

Although the maximum working pressure for the cell was 40 MPa, the current measurements were restricted to pressures below 20 MPa. This was due to the polyphenylene sulphide seals with low water absorption used in the ROLSI samplers, which provided leak-free sealing only up to that pressure.

2.3. Experimental Procedure

The static-analytical approach was used to determine the composition of the vapour and liquid phases coexisting in equilibrium. First, the apparatus was held under vacuum using a two-stage diaphragm pump until the pressure was below 1 kPa. Afterwards, the system was flushed with either N_2 or the (CO_2 + N_2) mixture. This procedure was repeated several times to remove impurities. The temperature controller was then adjusted to the desired value. As the temperature of the equilibrium cell reached the target value, a certain volume of water was pumped into the cell, and then N_2 or the (CO_2 + N_2) mixture was injected into the cell until a pressure of about 1 MPa was reached. The volume of water injected was chosen to ensure that the liquid sampling capillary was sufficiently immersed,

leaving space for the vapour phase. Then, the cell was isolated from the pump by closing the pneumatic valve, and the magnetic stirrer was switched on. The system was left to reach an equilibrium state, which was judged to have been attained when the pressure stabilised and reproducible sample compositions were obtained. At that point, the stirrer was stopped, the phases were sampled, starting with the aqueous phase and progressing to the gas phase. Tiny quantities of either the liquid or the vapour phase were sent from the pressurised cell to the online GC for analysis by opening the ROLSI samplers for a specific time, usually between 0.05 s and 2 s, depending on the phase and the system pressure. Around ten samples of each phase were taken for analysis. In the first five samples, the period between sample collection was less than 10 s in order to flush the capillary from any stagnant fluid. The analyses of these samples were discarded. For the following five samples, the period between sample collection was three minutes. The gas chromatographs were recorded over 30 min, which was the time necessary for the five samples to elute. The peak areas were tested for repeatability. In general, the standard relative deviations of successive peak area responses for water were below 5%. The pressure and temperature were recorded during the sampling time, and their mean and standard deviation were estimated. It was observed that the samples removed from the cell had an insignificant effect on the pressure during the analysis of a single equilibrium state.

The components of the sample were separated on an HP-Plot-Q column. The temperature of the column oven and detectors and the split-ratio and Deans-switch times were optimised to achieve fast analysis with satisfactory separation between eluates. The first eluate was nitrogen, followed by carbon dioxide and, finally, water. The major components of the sample were transferred to the TCD, and the minor components were passed to the PDHID by switching the DSS. The TCD signal had less than 0.5% noise, and the PDHID signal had less than 2% noise. A chromatogram for the (H_2O + N_2) binary system is shown in Figure 2. Table 4 details the detector used for each component in each phase for both the binary and ternary systems studied here. After determining the composition of two phases, additional gas was injected to increase the pressure for the next state point, up to a maximum of about 20 MPa. The vapour–liquid equilibria for the (H_2O + N_2) and (CO_2 + H_2O + N_2) systems were measured at temperatures between 323 and 473 K and at pressures up to 20.0 MPa.
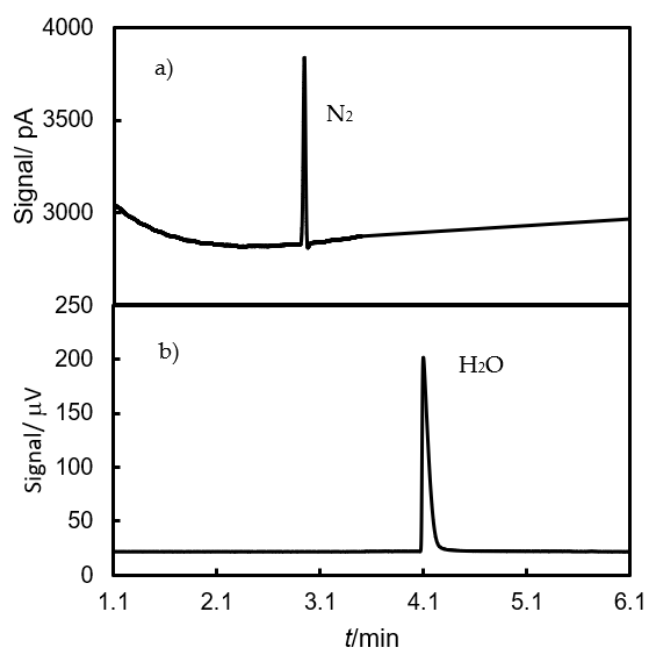
Figure 2. Gas chromatograph recorded on (**a**) PDHID and (**b**) TCD for the liquid phase of the (N_2 + H_2O) system. HP-Plot-Q column, 0.32 mm OD × 30 m length, film thickness 20 μm.

Table 4. For binary and ternary systems, the component that passed through the detector: thermal conductivity detector (TCD) or pulse-discharge helium ionisation detector (PDHID) (D-3-I-HP, Vici) in an Agilent 7890A GC with an HP-PLOT-Q capillary column.

System	Phase	TCD	PDHID
$H_2O + N_2$	Liquid phase	H_2O	N_2
	Vapour phase	N_2	H_2O
$CO_2 + H_2O$	Liquid phase	H_2O, CO_2	
	Vapour phase	CO_2	H_2O
$CO_2 + H_2O + N_2$	Liquid phase	CO_2, H_2O	N_2
	Vapour phase	CO_2, N_2	H_2O

2.4. GC Calibration

A modified peak–area ratio method was used to convert chromatographic peak areas into mole fractions. This method assumes that the amount, n_i, of substance i in the mixture is proportional to the corresponding chromatographic peak area, A_{wi}, measured on detector w, as follows:

$$n_i = k_{wi} A_{wi} \tag{1}$$

where k_{wi} is the response factors for component i on detector w. The mole fraction, x_i, of component i is determined as follows:

$$x_i = n_i \left[\sum_{j=1}^{N_c} n_k \right]^{-1} = k_{wi} A_{wi} \left[\sum_{j=1}^{N_c} k_{wj} A_{wj} \right]^{-1} \tag{2}$$

Thus, dividing both the numerator and the denominator by k_{wi},

$$x_i = \frac{A_{wi}}{\sum\limits_{j=1}^{N_c} r_{wj} A_{wj}} \tag{3}$$

where $r_{wj} = k_{wj}/k_{wi}$ is the relative response factor. Knowing the composition of a single calibration mixture, a series of relative response factors can be calculated by solving Equation (3) for each mixture component.

TCD and PDHID detectors are considered universal, non-destructive, concentration-sensitive detectors, and their responses are linear relative to the concentration [55,56]. In addition, vapour–liquid equilibrium data for the ($CO_2 + H_2O$) and ($H_2O + N_2$) binary systems have been extensively measured in the literature, and the results are quite consistent. Therefore, considering the detector linearity and the availability of accurate experimental data, the modified peak–area ratio method was employed with these mixtures as calibration systems.

As an illustration, for the case of the ($H_2O + N_2$) mixture, the mole fraction of nitrogen in the liquid phase, x_{N_2}, can be written as follows:

$$x_{N_2} = \frac{A_{PN_2}}{r_{TPN_2} A_{TH_2O} + A_{PN_2}} \tag{4}$$

Hence:

$$r_{TPN_2} = \frac{A_{PN_2} x_{H_2O}}{A_{TH_2O} x_{N_2}} \tag{5}$$

where $r_{TPN_2} = k_{TH_2O}/k_{PN_2}$ is the relative response factor; k_{TH_2O} is the response factor of the TCD to water, the major component in the mixture; and k_{PN_2} is the response factor of the PDHID to nitrogen, the minor component in the mixture. Additionally, A_{TH_2O} and A_{PN_2} are the chromatographic peak areas for water and nitrogen measured on the TCD and the PDHID, respectively. Table 5 details the obtained calibration data. The phase equilibrium

data published by Wiebe et al. [15] were selected to obtain the relative response factors because the reported data were judged to be accurate and were corroborated by multiple authors. The selected data point was 373.15 K, 10.0 MPa, at which $x_{N_2} = 0.00082$. The peak areas were obtained by sending ten consecutive samples from the equilibrium liquid phase of the ($H_2O + N_2$) system in the vessel at 10.0 MPa and 373.15 K to the GC. The uncertainties in the peak area were obtained in terms of response peak area reproducibility and are also shown in Table 4. A similar procedure was carried out to obtain relative response factors for the vapour phase of the ($H_2O + N_2$) system and for both phases of the ($CO_2 + H_2O$) system. The phase compositions for the ($CO_2 + H_2O$) system were obtained from the model developed by Spycher et al. [20].

In the ($CO_2 + H_2O + N_2$) system, the mole fractions can be obtained from Equation (3) using the relative response factors for the binary systems from Table 5. For example, the mole fraction of CO_2 in the liquid phase is given by:

$$x_{CO_2} = \frac{(1/r_{TTCO_2}) A_{TCO_2}}{(1/r_{TTCO_2}) A_{TCO_2} + A_{TH_2O} + (1/r_{TPN_2}) A_{PN_2}} \tag{6}$$

2.5. Uncertainty Analysis

The combined standard uncertainty of the mole fraction of each component in a given phase, $u(x_i)$, is derived from the following equation with reference to the description of uncertainty in measurements (GUM) [57].

$$u^2(x_i) = \sum_{j=1}^{n} \sum_{k=1}^{n} \frac{\partial x_i}{\partial z_j} \frac{\partial x_i}{\partial z_k} u^2(z_j, z_k) \tag{7}$$

where measured input variables are z_j and z_k; the sensitivity coefficient of the input variable, z_k, is $(\partial x_i / \partial z_k)$; and the covariance ($j \neq k$) or the variance ($j = k$) for variables z_j and z_k is $u^2(z_j, z_k)$.

In the present analysis, only the diagonal variance terms are considered. Using Equations (3) and (7), the overall combined standard uncertainty of the mole fraction resulting from temperature, pressure, relative response factor and chromatographic peak area uncertainties is then given by:

$$u^2(x_i) = \left(\frac{\partial x_i}{\partial T}\right)^2 u^2(T) + \left(\frac{\partial x_i}{\partial p}\right)^2 u^2(p) + \sum_{j=1}^{Nc} \left(\frac{\partial x_i}{\partial A_{wj}}\right)^2 u^2(A_{wj}) + \sum_{j=1}^{Nc} \left(\frac{\partial x_i}{\partial r_{wj}}\right)^2 u^2(r_{wj}) \tag{8}$$

The standard uncertainty in the relative response factor, considering Equation (4), is given by:

$$u^2(r_{wj}) = \left[\sum_{k=1}^{N_c} \left(\frac{\partial r_{wj}}{\partial A_{wk}}\right)^2 u^2(A_{wk}) + \sum_{j=1}^{N_c} \left(\frac{\partial r_{wj}}{\partial x_k}\right)^2 u^2(x_k) \right]_{Cal} \tag{9}$$

where subscript "cal" denotes the calibration measurement. The relative response factor for binary mixtures was estimated by the uncertainties of both peak areas and mole fractions, the latter being recorded in the literature, and is influenced by pressure and temperature uncertainties. The $u(r_{wj})$ values are shown in Table 5. The total combined standard uncertainties of mole fraction ranged from $1 \cdot 10^{-6}$ to $3 \cdot 10^{-3}$, depending on the temperature, pressure, component and phase.

Table 5. Relative response factor, r; response factor, k; and chromatographic peak areas, A. The subscripts T and P indicate TCD and PDHID detectors, respectively. Literature data of the binary mixture.

System	Phase	Relative Response Factors			Peak Area						Ref
			$r_{TPN_2}/$ $(pA\cdot\mu V)$	$u(r_{TPN_2})/$ $(pA\cdot\mu V)$	$A_{TH_2O}/$ $(\mu V\cdot min)$	$u(A_{TH_2O})/$ $(\mu V\cdot min)$	$A_{PN_2}/$ $(pA\cdot min)$	$u(A_{PN_2})/$ $(pA\cdot min)$	x_{N_2}	
$H_2O + N_2$	Liquid	$r_{TPN_2} = \frac{k_{TH_2O}}{k_{PN_2}}$	4672	45	327	2	1250	10	0.00082	[15]
			$r_{TN_2P}/$ $(pA\cdot\mu V)$	$u(r_{TN_2P})/$ $(pA\cdot\mu V)$	$A_{PH_2O}/$ $(pA\cdot min)$	$u(A_{PH_2O})/$ $(pA\cdot min)$	$A_{TN_2}/$ $(\mu V\cdot min)$	$u(A_{TN_2})/$ $(\mu V\cdot min)$	y_{H_2O}	
	Vapour	$r_{TN_2P} = \frac{k_{TN_2}}{k_{PH_2O}}$	3443	161	13,420	552	498	1	0.00777	[19]
			r_{TTCO_2}	$u(r_{TTCO_2})$	$A_{TH_2O}/$ $(\mu V\cdot min)$	$u(A_{TH_2O})/$ $(\mu V\cdot min)$	$A_{TCO_2}/$ $(\mu V\cdot min)$	$u(A_{TCO_2})/$ $(\mu V\cdot min)$	x_{CO_2}	
$CO_2 + H_2O$	Liquid	$r_{TTCO_2} = \frac{k_{TH_2O}}{k_{TCO_2}}$	2.12	0.01	793	4	23.7	0.1	0.01393	[20]
			$r_{TCO_2P}/$ $(pA\cdot\mu V)$	$u(r_{TCO_2P})/$ $(pA\cdot\mu V)$	$A_{PH_2O}/$ $(pA\cdot min)$	$u(A_{PH_2O})/$ $(pA\cdot min)$	$A_{TCO_2}/$ $(\mu V\cdot min)$	$u(A_{TCO_2})/$ $(\mu V\cdot min)$	y_{H_2O}	
	Vapour	$r_{TCO_2P} = \frac{k_{TCO_2}}{k_{PH_2O}}$	3209	102	28,920	733	358	1	0.02453	[20]

2.6. Validation

To validate the calibration, vapour–liquid equilibrium data for the (CO_2 + H_2O) mixture were measured at several different pressures on the isotherm at T = 373 K (the data at p = 10 MPa being used for calibration). Table 6 and Figure 3 show the results. The data were compared with the model reported by Spycher et al. [20,58] and are in good agreement with an absolute average deviation (Δ_{AAD}) of the CO_2 mole fraction equal to $1.8 \cdot 10^{-4}$ and $9.8 \cdot 10^{-4}$ for the liquid and vapour phases, respectively. The deviations were within our uncertainties, which are given in Table 6.

Table 6. Experimental vapour–liquid equilibrium data for the $CO_2(1)$ + $H_2O(2)$ systems at 373 K and up to 15 MPa. x represents mole fraction in the liquid phase, y denotes mole fraction in the gas phase and u denotes standard uncertainty.

Liquid Phase						Vapour Phase					
T/K	*u(T)*	*p/MPa*	*u(p)*	x_1	$u(x_1)$	*T/K*	*u(T)*	*p/MPa*	*u(p)*	y_1	$u(y_1)$
373.28	0.02	4.71	0.01	0.00780	$1.58 \cdot 10^{-4}$	373.27	0.02	4.71	0.01	0.97323	$1.35 \cdot 10^{-3}$
373.26	0.01	5.45	0.01	0.00899	$4.51 \cdot 10^{-4}$	373.27	0.02	4.70	0.01	0.97370	$1.49 \cdot 10^{-3}$
373.28	0.01	10.07	0.01	0.01434	$1.34 \cdot 10^{-4}$	373.27	0.02	5.46	0.01	0.97644	$1.33 \cdot 10^{-3}$
373.22	0.01	10.03	0.01	0.01393	$1.09 \cdot 10^{-4}$	373.27	0.02	5.45	0.01	0.97444	$1.01 \cdot 10^{-3}$
373.28	0.01	15.09	0.01	0.01784	$1.89 \cdot 10^{-4}$	373.27	0.01	10.06	0.01	0.98064	$6.29 \cdot 10^{-4}$
373.28	0.01	15.09	0.01	0.01822	$1.80 \cdot 10^{-4}$	373.28	0.01	10.04	0.01	0.98141	$5.29 \cdot 10^{-4}$
						373.27	0.01	15.09	0.01	0.98390	$4.33 \cdot 10^{-4}$
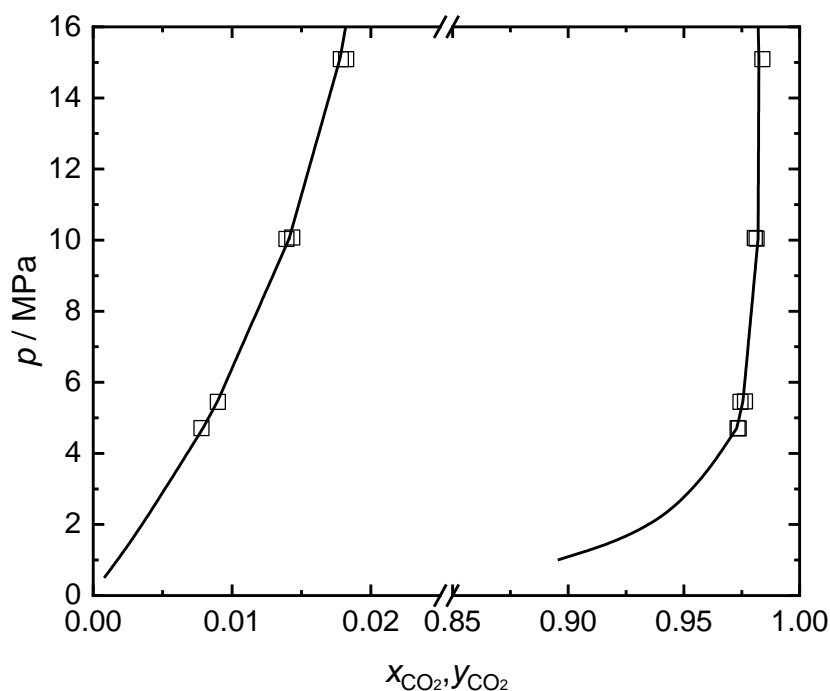
Figure 3. Vapour–liquid equilibrium for $CO_2(1)$ + $H_2O(2)$ systems at 373 K. Symbols represent the experimental data measured in this work, and the black line is the model reported by Spycher et al. [20].

3. Results

3.1. (H_2O + N_2) System

The vapour–liquid equilibrium data for the (H_2O + N_2) system were measured at temperatures of 323 K, 348 K, 373 K and 423 K at pressures up to 20 MPa. The experimental data and their estimated standard uncertainties are given in Tables 7 and 8. The phase behaviour is shown in Figure 4. The solubility of nitrogen in the aqueous phase increased as pressure rose at a constant temperature, whereas the water concentration in the gas

phase decreased. Under constant pressure, the water mole fraction in the vapour phase consistently increased with increasing temperature, as predicted. On the contrary, the solubility of nitrogen in the aqueous phase first decreased as temperature increased until a minimum of solubility was reached, after which it began to increase again. Figure 5 shows the solubility of nitrogen as a function of temperature at three pressures to better demonstrate this behaviour. The solubility minimum occurs at approximately T = 343 K and becomes more pronounced as pressure increases. This minimum of solubility has been reported for other water + gas systems, such as H_2O + CH_4 [59] and H_2O + CO_2 [46]. The (H_2O + N_2) system shows type III phase behaviour according to the classification of Scott and van Konynenburg [60], so there is not a continuous critical locus connecting the critical points of H_2O and N_2. At high temperatures, the critical line starts at the critical point of water (647.10 K and 22.064 MPa [61]) and, with increasing pressure, passes through a minimum of temperature, after which it increases steadily to temperatures above the water critical temperature, with gas–gas immiscibility of the second kind [32,62,63]. This system shows a large two-phase vapour–liquid equilibrium region, where our experimental measurements were conducted. The available literature data are also illustrated in Figures 4 and 5, and it can be seen that our data are in agreement with those reported in the literature.

Table 7. Experimental liquid-phase data for the $H_2O(1)$ + $N_2(2)$ system at different temperatures, T, and pressures, p. x and u denote the mole fraction in the liquid phase and standard uncertainty, respectively.

T/K	$u(T)$	p/MPa	$u(p)$	x_1	$u(x_1)$	x_2	$u(x_2)$
323.21	0.01	1.19	0.01	0.99988	0.00002	0.00012	0.00002
323.22	0.02	2.03	0.01	0.99984	0.00002	0.00016	0.00002
323.20	0.02	2.62	0.01	0.99979	0.00001	0.00021	0.00001
323.19	0.02	2.62	0.01	0.99977	0.00001	0.00023	0.00001
323.22	0.02	5.06	0.01	0.99958	0.00003	0.00042	0.00003
323.21	0.02	5.11	0.01	0.99958	0.00001	0.00042	0.00001
323.20	0.02	7.46	0.01	0.99939	0.00003	0.00061	0.00003
323.20	0.02	7.98	0.01	0.99937	0.00001	0.00063	0.00001
323.21	0.02	9.85	0.01	0.99919	0.00002	0.00081	0.00002
323.20	0.02	9.86	0.01	0.99919	0.00001	0.00081	0.00001
323.21	0.02	9.99	0.01	0.99916	0.00002	0.00084	0.00002
323.19	0.02	11.63	0.01	0.99909	0.00002	0.00091	0.00003
323.20	0.02	12.65	0.01	0.99897	0.00002	0.00103	0.00002
323.20	0.02	15.12	0.01	0.99884	0.00002	0.00116	0.00002
323.21	0.02	15.57	0.01	0.99884	0.00002	0.00116	0.00002
323.20	0.02	17.63	0.01	0.99868	0.00002	0.00132	0.00002
323.20	0.02	20.20	0.01	0.99851	0.00004	0.00149	0.00004
348.30	0.02	0.95	0.01	0.99992	0.00000	0.00008	0.00000
348.33	0.02	1.02	0.01	0.99992	0.00000	0.00008	0.00000
348.30	0.02	1.87	0.01	0.99985	0.00000	0.00015	0.00000
348.30	0.02	5.26	0.01	0.99957	0.00001	0.00043	0.00001
348.30	0.02	7.46	0.01	0.99938	0.00001	0.00062	0.00001
348.30	0.02	10.02	0.01	0.99920	0.00003	0.00080	0.00003
348.28	0.01	12.51	0.01	0.99899	0.00001	0.00101	0.00001
373.22	0.01	1.22	0.01	0.99993	0.00001	0.00007	0.00001
373.17	0.02	1.52	0.01	0.99989	0.00002	0.00011	0.00002
373.17	0.02	2.46	0.01	0.99980	0.00003	0.00020	0.00003
373.22	0.01	5.03	0.01	0.99961	0.00001	0.00039	0.00001
373.27	0.01	5.07	0.01	0.99961	0.00001	0.00039	0.00001
373.18	0.01	5.15	0.01	0.99958	0.00003	0.00042	0.00003
373.19	0.02	7.51	0.01	0.99937	0.00001	0.00063	0.00001
373.27	0.01	7.69	0.01	0.99937	0.00002	0.00063	0.00002
373.18	0.02	10.05	0.01	0.99918	0.00007	0.00082	0.00007

Table 7. *Cont.*

T/K	$u(T)$	p/MPa	$u(p)$	x_1	$u(x_1)$	x_2	$u(x_2)$
373.26	0.01	10.46	0.01	0.99918	0.00001	0.00082	0.00001
373.19	0.01	12.94	0.01	0.99894	0.00002	0.00106	0.00002
373.27	0.02	13.43	0.01	0.99893	0.00003	0.00107	0.00003
373.19	0.02	15.02	0.01	0.99881	0.00005	0.00119	0.00005
373.26	0.01	15.04	0.01	0.99879	0.00002	0.00121	0.00002
373.25	0.01	17.56	0.01	0.99863	0.00018	0.00137	0.00018
373.19	0.02	17.67	0.01	0.99861	0.00002	0.00139	0.00002
373.19	0.02	20.48	0.01	0.99846	0.00005	0.00154	0.00005
423.01	0.02	1.55	0.01	0.99991	0.00001	0.00009	0.00001
423.31	0.02	1.70	0.01	0.99988	0.00000	0.00012	0.00000
423.41	0.01	2.51	0.01	0.99980	0.00001	0.00020	0.00001
422.92	0.02	2.57	0.01	0.99978	0.00001	0.00022	0.00001
423.22	0.02	5.40	0.01	0.99950	0.00002	0.00050	0.00002
423.22	0.02	7.59	0.01	0.99934	0.00002	0.00066	0.00002
423.22	0.02	10.37	0.01	0.99906	0.00003	0.00094	0.00003
423.22	0.02	12.64	0.01	0.99884	0.00003	0.00116	0.00003
423.21	0.02	15.30	0.01	0.99861	0.00002	0.00139	0.00002
423.22	0.02	17.57	0.01	0.99847	0.00002	0.00153	0.00002
423.22	0.02	20.59	0.01	0.99815	0.00004	0.00185	0.00004

Table 8. Experimental vapour-phase data for the $H_2O(1) + N_2(2)$ system at different temperatures, T, and pressures p. y and u denote the mole fraction of water in the vapour phase and standard uncertainty, respectively.

T/K	$u(T)$	p/MPa	$u(p)$	y_1	$u(y_1)$	y_2	$u(y_2)$
323.22	0.02	1.21	0.01	0.01238	0.00075	0.98762	0.00074
323.20	0.02	2.03	0.01	0.00742	0.00016	0.99258	0.00016
323.21	0.02	5.04	0.01	0.00291	0.00005	0.99709	0.00005
323.21	0.02	6.22	0.01	0.00241	0.00028	0.99759	0.00028
323.21	0.02	7.94	0.01	0.00183	0.00001	0.99817	0.00001
323.22	0.02	15.32	0.01	0.00161	0.00002	0.99839	0.00002
373.22	0.01	1.22	0.01	0.08956	0.00269	0.91044	0.00261
373.23	0.01	1.22	0.01	0.08679	0.00314	0.91321	0.00308
373.23	0.01	1.22	0.01	0.08203	0.00446	0.91797	0.00442
373.26	0.01	2.59	0.01	0.04247	0.00171	0.95753	0.00171
373.27	0.02	5.00	0.01	0.02187	0.00090	0.97813	0.00090
373.31	0.01	7.22	0.02	0.01451	0.00101	0.98549	0.00101
373.27	0.01	7.69	0.01	0.01350	0.00084	0.98650	0.00084
373.26	0.02	10.47	0.01	0.01284	0.00067	0.98716	0.00067
373.26	0.01	13.46	0.02	0.00861	0.00038	0.99139	0.00039
373.27	0.01	13.52	0.01	0.00855	0.00059	0.99145	0.00059
373.26	0.01	15.05	0.01	0.00864	0.00046	0.99136	0.00050
373.25	0.01	17.56	0.01	0.00762	0.00063	0.99238	0.00063
373.27	0.02	20.29	0.06	0.00678	0.00024	0.99322	0.00025
423.01	0.01	1.55	0.01	0.27129	0.01175	0.72871	0.01166
423.01	0.01	1.55	0.01	0.24613	0.01416	0.75387	0.01408
423.39	0.01	2.51	0.01	0.15648	0.00641	0.84352	0.00638
423.23	0.01	5.19	0.01	0.08907	0.00282	0.91093	0.00282
423.23	0.01	7.64	0.01	0.06089	0.00263	0.93911	0.00263
423.25	0.02	9.97	0.01	0.05784	0.00335	0.94216	0.00335
423.26	0.01	12.70	0.01	0.04426	0.00248	0.95574	0.00248
423.26	0.02	15.18	0.01	0.03558	0.00192	0.96442	0.00192
423.26	0.02	17.56	0.01	0.02868	0.00183	0.97132	0.00183
423.26	0.02	20.35	0.01	0.02606	0.00168	0.97394	0.00168
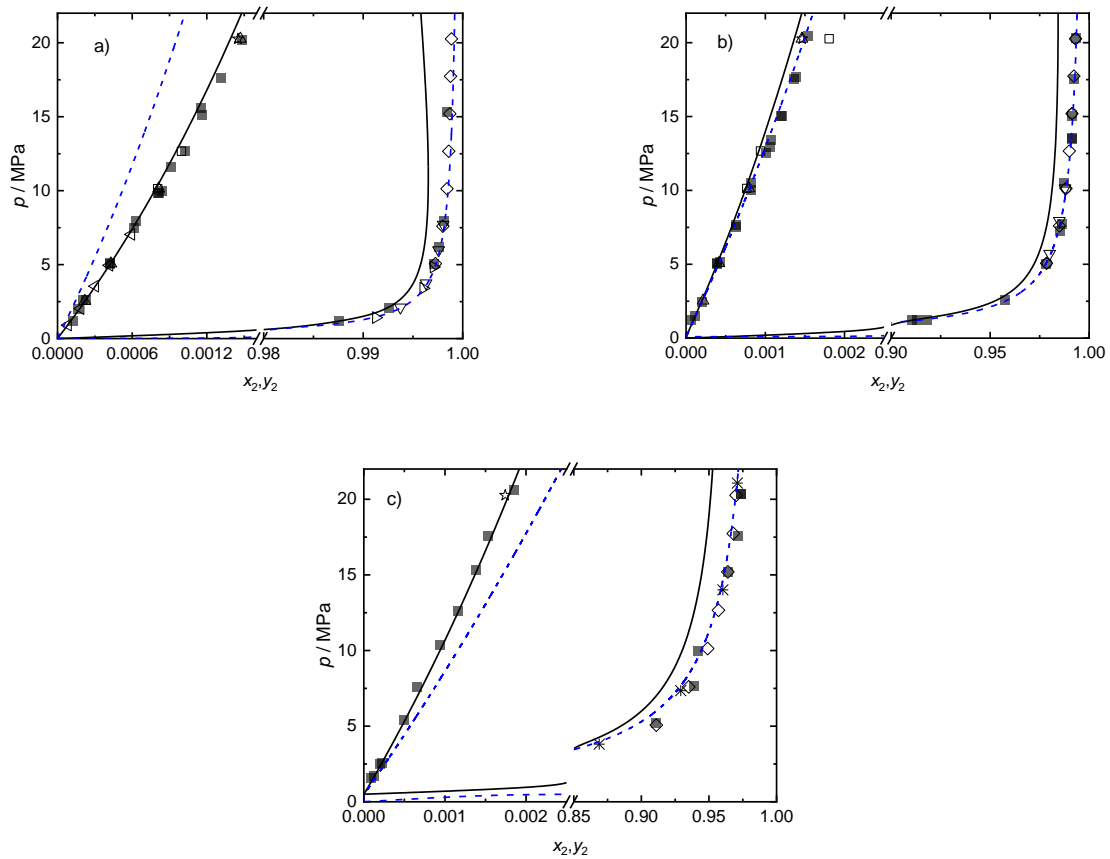
Figure 4. Vapour–liquid equilibrium for the ($H_2O(1)$ + $N_2(2)$) system at temperatures of (**a**) 323 K, (**b**) 373 K and (**c**) 423 K. Experimental data: ■, this work; □, Goodman and Krase [24]; △; Wiebe et al. [15]; ✰, Saddington and Krase [25]; ■, Sidorov et al. [26]; ▽, Rigby and Prausnitz [18]; ◇, Maslennikova et al. [19]; ◁, Chapoy et al. [39]; ▷, Mohammadi et al. [17]; and ✳, Tabasinejad et al. [40]. The continuous lines represent the description of the γ-φ model, and dashed lines represent the description of the SAFT-γ Mie model.
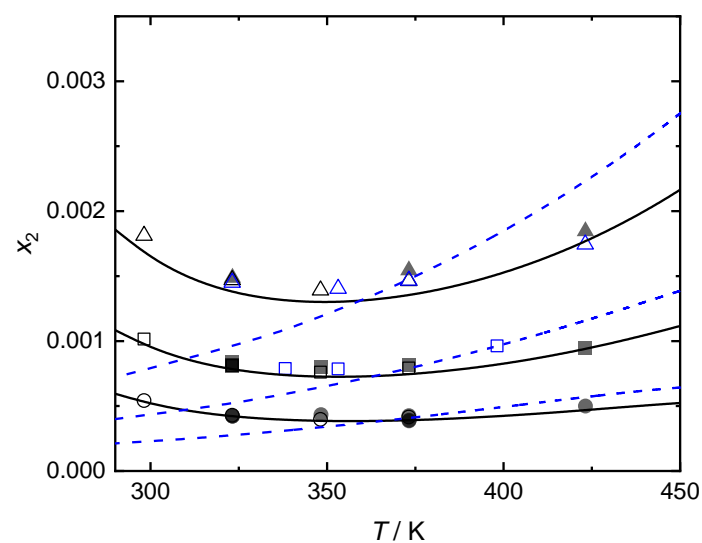

Figure 5. Solubility data of nitrogen in the aqueous phase as a function of temperature for the ($H_2O(1)$ + $N_2(2)$) system at pressures of ●, 5 MPa; ■, 10 MPa; ▲, 20 MPa. The filled symbols denote data from this work, and empty symbols represent data from the literature: black, Wiebe et al. [15]; blue, Saddington and Krase [25]. The continuous lines represent the description of the γ-φ model, and dashed lines represent the description of the SAFT-γ Mie model.

3.2. (CO$_2$ + H$_2$O + N$_2$) System

The vapour–liquid equilibrium for the ternary system was measured along four isotherms ranging from 323 K to 473 K in increments of 50 K and at pressures up to 20.0 MPa. The mole ratio between carbon dioxide and nitrogen injected as gas into the system was unity. The experimental data are given in Table 9 and plotted in pressure-composition diagrams in Figures 6 and 7. The solubility of CO$_2$ and N$_2$ increased with increasing pressure. The nitrogen solubility increased with increasing temperature, whereas the CO$_2$ solubility decreased. Overall, the total gas solubility (CO$_2$ and N$_2$ combined) decreased with temperature. No minimum solubility was observed for the ternary system, as observed with the (H$_2$O + N$_2$) system. On the other hand, the water concentration in the vapour phase increased with temperature and decreased with pressure, as expected.

**Table 9.** Experimental vapour–liquid equilibrium data for the $[CO_2(1) + H_2O(2) + N_2(3)]$ system at different temperatures, T, and pressures, p. x and y denote the mole fraction in the liquid and vapour phase, respectively. u is the standard uncertainty.

Liquid Phase										Vapour Phase									
T/K	$u(T)$	p/MPa	$u(p)$	x_1	$u(x_1)$	x_2	$u(x_2)$	x_3	$u(x_3)$	T/K	$u(T)$	p/MPa	$u(p)$	y_1	$u(x_1)$	y_2	$u(x_2)$	y_3	$u(x_3)$
323.21	0.01	1.44	0.01	0.00170	0.00011	0.99827	0.00011	0.00003	0.00000	323.22	0.02	1.45	0.01	0.37463	0.01410	0.01015	0.00057	0.61522	0.01405
323.21	0.01	2.36	0.02	0.00270	0.00007	0.99721	0.00007	0.00009	0.00000	323.21	0.02	2.34	0.01	0.38050	0.01416	0.00634	0.00039	0.61316	0.01413
323.19	0.01	4.86	0.02	0.00457	0.00012	0.99526	0.00012	0.00017	0.00001	323.19	0.02	4.86	0.01	0.39579	0.01427	0.00376	0.00026	0.60044	0.01424
323.20	0.01	7.29	0.01	0.00624	0.00015	0.99352	0.00016	0.00023	0.00001	323.20	0.02	7.27	0.01	0.40599	0.01437	0.00300	0.00016	0.59101	0.01434
323.19	0.01	9.71	0.02	0.00763	0.00034	0.99208	0.00035	0.00029	0.00002	323.18	0.02	9.71	0.02	0.42363	0.01450	0.00186	0.00011	0.57451	0.01444
323.18	0.01	12.71	0.02	0.00881	0.00060	0.99085	0.00060	0.00034	0.00001	323.17	0.02	12.75	0.01	0.42779	0.01455	0.00177	0.00011	0.57044	0.01444
										323.18	0.02	15.50	0.01	0.43245	0.01473	0.00188	0.00012	0.56567	0.01449
323.18	0.01	20.09	0.02	0.01260	0.00030	0.98679	0.00030	0.00061	0.00002	323.19	0.02	20.03	0.01	0.44026	0.01508	0.00185	0.00014	0.55789	0.01451
373.26	0.01	2.51	0.01	0.00174	0.00015	0.99819	0.00015	0.00007	0.00001	373.27	0.01	2.50	0.01	0.38941	0.01429	0.04366	0.00179	0.56693	0.01398
373.27	0.01	5.21	0.01	0.00366	0.00004	0.99615	0.00004	0.00019	0.00001	373.27	0.01	5.14	0.01	0.42016	0.01426	0.02032	0.00072	0.55952	0.01406
373.28	0.02	7.39	0.01	0.00503	0.00018	0.99467	0.00018	0.00030	0.00001	373.28	0.01	7.36	0.01	0.42944	0.01430	0.01692	0.00057	0.55364	0.01413
373.26	0.02	10.04	0.01	0.00645	0.00009	0.99314	0.00009	0.00041	0.00001	373.27	0.02	10.03	0.01	0.43615	0.01437	0.01446	0.00052	0.54939	0.01422
373.28	0.02	12.53	0.01	0.00765	0.00029	0.99181	0.00029	0.00054	0.00002	373.28	0.02	12.48	0.01	0.43873	0.01440	0.01226	0.00046	0.54902	0.01427
373.25	0.01	14.86	0.01	0.00828	0.00023	0.99110	0.00024	0.00063	0.00003	373.27	0.02	14.79	0.02	0.43837	0.01440	0.00960	0.00033	0.55203	0.01429
373.24	0.02	14.92	0.01	0.00821	0.00018	0.99118	0.00019	0.00061	0.00001	373.24	0.01	14.87	0.01	0.43752	0.01440	0.01087	0.00043	0.55161	0.01428
373.28	0.01	17.44	0.01	0.00902	0.00055	0.99024	0.00057	0.00074	0.00004	373.27	0.02	17.47	0.02	0.43964	0.01440	0.00871	0.00031	0.55165	0.01430
373.26	0.01	19.96	0.01	0.00972	0.00260	0.98941	0.00272	0.00087	0.00023	373.27	0.01	19.81	0.02	0.44095	0.01445	0.00905	0.00032	0.55000	0.01435
423.45	0.02	1.51	0.01	0.00062	0.00006	0.99936	0.00006	0.00002	0.00000	423.46	0.02	1.52	0.01	0.34918	0.01254	0.2668	0.00445	0.3841	0.01135
423.45	0.02	2.44	0.01	0.00122	0.00015	0.99873	0.00016	0.00005	0.00001										
										423.27	0.01	2.67	0.01	0.39535	0.01338	0.1803	0.00339	0.4244	0.01248
423.67	0.02	4.89	0.01	0.00253	0.00023	0.99728	0.00024	0.00019	0.00002										
423.27	0.02	4.97	0.01	0.00284	0.00011	0.99694	0.00011	0.00022	0.00002	423.26	0.02	4.94	0.01	0.42967	0.01377	0.1115	0.00200	0.4588	0.01319
423.66	0.02	9.89	0.01	0.00533	0.00007	0.99427	0.00007	0.00040	0.00001	423.66	0.02	9.85	0.01	0.45373	0.01408	0.0680	0.00128	0.4783	0.01371
423.29	0.02	12.55	0.01	0.00644	0.00017	0.99304	0.00018	0.00052	0.00001	423.28	0.03	12.52	0.01	0.45747	0.01413	0.0572	0.00113	0.4853	0.01383
423.28	0.02	15.06	0.01	0.00729	0.00016	0.99210	0.00017	0.00062	0.00001	423.28	0.03	15.02	0.01	0.46251	0.01419	0.0478	0.00093	0.4897	0.01393
423.29	0.02	20.60	0.01	0.00926	0.00030	0.98990	0.00031	0.00084	0.00002	423.27	0.02	19.82	0.02	0.46937	0.01423	0.0419	0.00154	0.4887	0.01399
472.90	0.03	2.81	0.03	0.00080	0.00004	0.99914	0.00004	0.00005	0.00001	472.90	0.02	2.80	0.01	0.2772	0.01276	0.4170	0.01043	0.3058	0.01168
										472.90	0.02	2.79	0.01	0.2402	0.01403	0.4953	0.01986	0.2644	0.01377
472.91	0.02	4.87	0.02	0.00210	0.00012	0.99768	0.00012	0.00022	0.00002	472.92	0.03	4.88	0.01	0.3487	0.01401	0.2701	0.01060	0.3812	0.01316
472.91	0.03	9.63	0.03	0.00487	0.00010	0.99465	0.00011	0.00048	0.00002	472.92	0.02	9.58	0.01	0.4065	0.03015	0.1539	0.00818	0.4395	0.03046
472.91	0.02	15.33	0.02	0.00765	0.00016	0.99129	0.00017	0.00106	0.00005	472.93	0.03	15.34	0.01	0.3997	0.02187	0.1307	0.00529	0.4695	0.02167
472.93	0.03	20.12	0.03	0.00955	0.00039	0.98916	0.00040	0.00129	0.00002	472.92	0.02	20.11	0.01	0.3918	0.02897	0.1240	0.01023	0.4842	0.02890
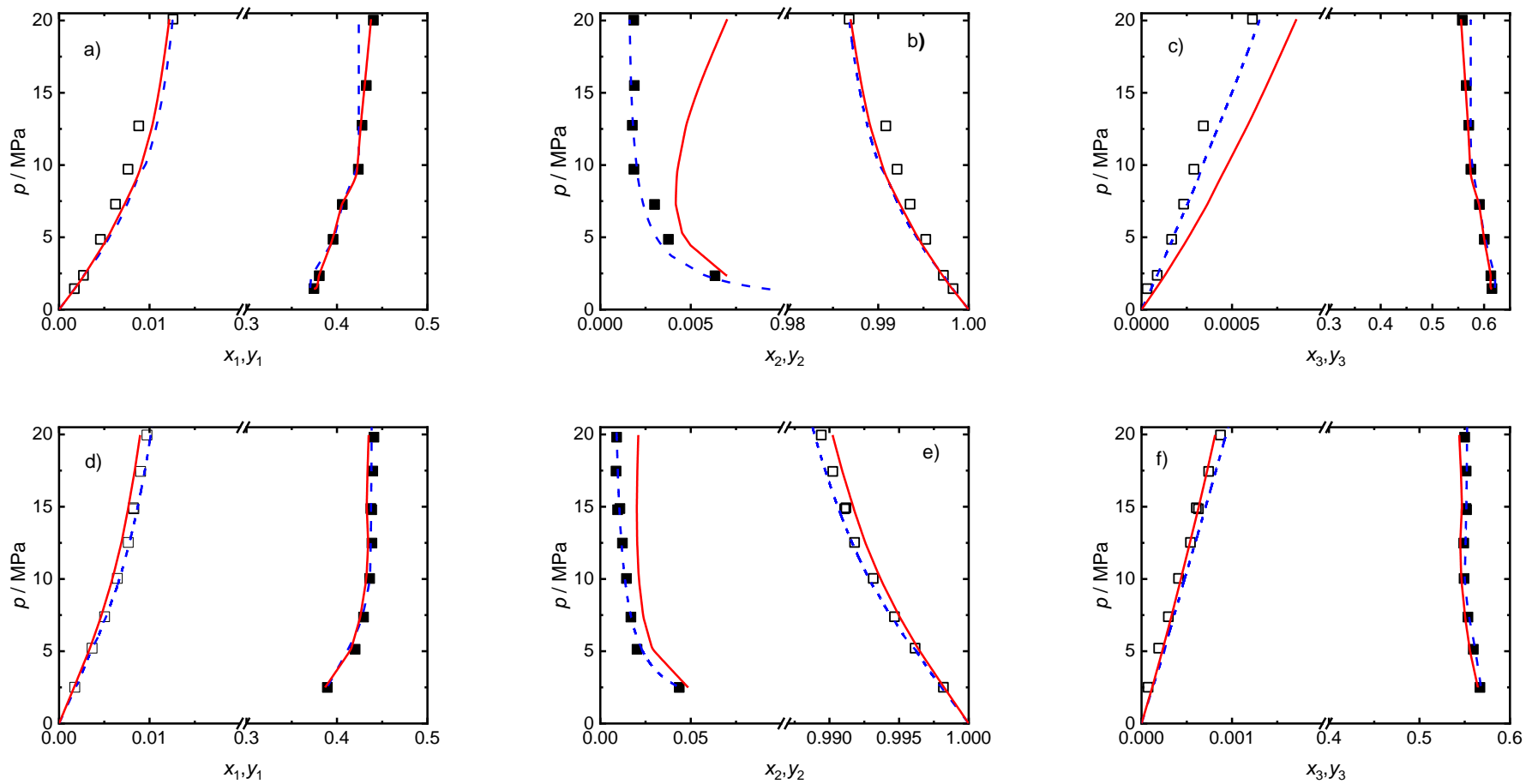
Figure 6. Vapour–liquid equilibrium for the (CO_2(1) + H_2O(2) +N_2(3)) system at temperatures of (**a–c**) 323 K and (**d–f**) 373 K. Empty symbols represent dew points, and filled-in symbols represent bubble points. The mole ratio of CO_2/N_2 fed to the system was 1. Continuous red lines represent the description of the γ-φ model, and dashed blue lines represent the description of the SAFT-γ Mie model.
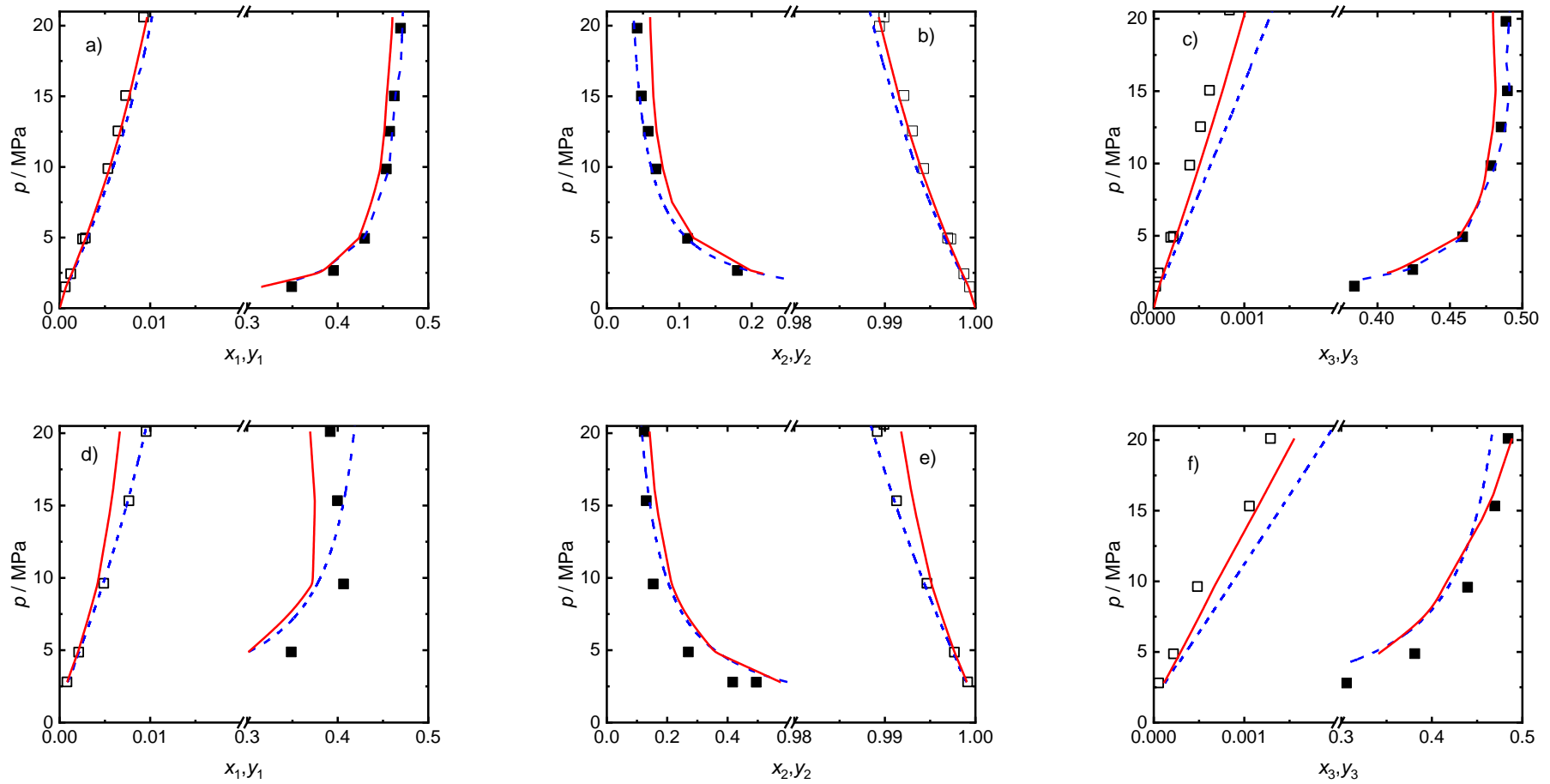
Figure 7. Vapour–liquid equilibrium for the (CO_2(1) + H_2O(2) +N_2(3)) system at temperatures of (**a–c**) 423 K and (**d–f**) 473 K. Empty symbols represent dew points, and filled-in symbols represent bubble points. The mole ration of CO_2/N_2 fed to the system was 1. Continuous red lines represent the description of the γ-φ model, and dashed blue lines represent the description of the SAFT-γ Mie model.

4. Thermodynamic Modelling

4.1. γ-φ Model

In this work, the phase behaviour of the (H_2O + N_2) and (CO_2 + H_2O + N_2) systems was modelled using the approach reported by Hou et al. [46] based on the asymmetrical γ-φ approach. In this model, the vapour phase is described by the Peng–Robinson equation of state (PR-EoS), whereas the aqueous phase is described by the NRTL activity coefficient model combined with an extended form of Henry's law.

In the model of Hou et al. [46], the equality of fugacity for CO_2 and N_2 is expressed as:

$$y_i \phi_i p = x_i \gamma_i^* H_{ij} \exp\left(\frac{V_i^\infty(p - p^{\text{ref}})}{RT}\right) \tag{10}$$

where R is the universal gas constant; T is the equilibrium temperature; p is the equilibrium pressure; x_i and y_i are mole fractions for the liquid and vapour phase, respectively; φ_i is the fugacity coefficient in the vapour phase; γ_i^* is the activity coefficient normalised to unity at infinite dilution; H_{ij} is Henry's constant for component i in aqueous solution; p^{ref} is the reference pressure; and V_i^∞ is the partial molar volume at infinite dilution in aqueous solution. The subscript i denotes the solute, either N_2 or CO_2, and subscript j denotes the solvent H_2O. In this model, $V_{N_2}^\infty$ was obtained from Mao and Duan [64], and $V_{CO_2}^\infty$ was obtained from the approach of Sedlbauer et al. [65]. Henry's constant for CO_2 in the aqueous solution was obtained from Hou et al. [46] whereas, for N_2 in aqueous solution, it was obtained from Fernández-Prini et al. [66]. The reference pressure, p^{ref}, was set as the vapour pressure of pure H_2O at temperature T.

For H_2O, the equality of fugacity is expressed as:

$$y_j \phi_j p = x_j \gamma_j \phi_j^{\text{sat}} p_j^{\text{sat}} \exp\left(\frac{V_j^{\text{sat}}(p - p^{\text{ref}})}{RT}\right) \tag{11}$$

Here, γ_j is the activity coefficient of H_2O; ϕ_j^{sat}, p_j^{sat} and V_j^{sat} are the fugacity coefficient, vapour pressure and liquid molar volume for pure saturated water, respectively; ϕ_j^{sat}, p_j^{sat} and V_j^{sat} were obtained from REFPROP 10 [61].

The activity coefficients are represented in this model by the NRTL equation [67]. The interaction parameters between H_2O and N_2 in the NRTL model were set to zero so that γ_{H_2O} and $\gamma_{N_2}^*$ were unity in the (N_2 + H_2O) binary system. For (CO_2 + H_2O), the NRTL interaction parameters were taken from Hou et al. [46].

The PR-EoS is given by:

$$p(T, v) = \frac{RT}{v - b} - \frac{a(T)}{v(v + b) + b(v - b)} \tag{12}$$

where v is molar volume, a is the attractive energy parameter and b is the co-volume parameter. The following equations are used to calculate a and b for individual components:

$$\left.\begin{aligned}
&a_i = 0.457236\left(R^2 T_{\text{c},i}^2 / p_{\text{c},i}\right)\alpha_i(T) \\
&\alpha_i(T) = \left[1 + m_i\left(1 - \sqrt{T/T_{\text{c},i}}\right)\right]^2 \\
&\omega_i \leq 0.491\ m_i = 0.37464 + 1.54226\omega_i - 0.26992\omega_i^2 \\
&\omega_i > 0.491\ m_i = 0.379642 + 1.48503\omega_i - 0.164423\omega_i^2 + 0.01666\omega_i^3 \\
&b_i = 0.077796(RT_{\text{c},i} / p_{\text{c},i})
\end{aligned}\right\} \tag{13}$$

In Equation (13), $T_{\text{c},i}$, $p_{\text{c},i}$ and ω_i are the critical temperature, critical pressure and acentric factors, respectively, of component i. The critical parameters and acentric factor were obtained from the REFPROP 10 [61], and they are listed in Table 10.

Table 10. Critical temperature, T_c, critical pressure, p_c, and acentric factor, ω, for CO_2, H_2O and N_2 used in the PR-EOS [61].

Component	T_c/K	p_c/MPa	ω
CO_2	304.13	7.3773	0.22394
H_2O	647.10	22.064	0.3443
N_2	126.19	3.3958	0.0372

The van der Waals mixing rules are applied to the Peng–Robinson EoS for mixtures:

$$\left. \begin{aligned} a &= \sum_{i=1}^{N} \sum_{j=1}^{N} x_i x_j \left[1 - k_{ij}(T) \right] \sqrt{a_i a_j} \\ b &= \sum_{i=1}^{N} x_i b_i \end{aligned} \right\} \tag{14}$$

where $k_{ij}(T) = k_{ji}(T)$ is the binary interaction parameter between components i and j, and x_i is the mole fraction of component i. In this model, $k_{ij}(T)$ is a linear function of the temperature. The $k_{ij}(T)$ in the PR-EoS for (N_2 + H_2O) was taken from Abudour et al. [68], that for (CO_2 + H_2O) was taken from Hou et al. [46] and that for CO_2 + N_2 was taken from Mantovani et al. [69]. The thermodynamic parameters used in the γ-φ model are summarised in [70]. The model was written in Visual Basic for applications within an Excel spreadsheet platform.

4.2. SAFT-γ Mie Equation of State

Papaioannou et al. [71] described the SAFT-γ Mie model in-depth, and so we outline only the energy interaction and the nature and source of the parameters employed here. The molecules in SAFT-γ Mie are represented as heteronuclear chains of fused spherical segments that interact based on the Mie potential [50,71–74], which is described as follows:

$$u_{kl}(r_{kl}) = \left(\frac{\lambda_{kl}^{r} \varepsilon_{kl}}{\lambda_{kl}^{r} - \lambda_{kl}^{a}} \right) \left(\frac{\lambda_{kl}^{r}}{\lambda_{kl}^{a}} \right)^{\lambda_{kl}^{a}/(\lambda_{kl}^{r} - \lambda_{kl}^{a})} \left[\left(\frac{\sigma_{kl}}{r_{kl}} \right)^{\lambda_{kl}^{r}} - \left(\frac{\sigma_{kl}}{r_{kl}} \right)^{\lambda_{kl}^{a}} \right] \tag{15}$$

The potential energy of the interaction between segments k and l, which represent functional groups in the molecule, is represented by U_{kl}. ε_{kl} is the energy parameter; λ_{kl}^{r} and λ_{kl}^{a} are the repulsive and attractive exponents, respectively; r_{kl} is the distance between the two groups; and σ_{kl} is the size parameter. The shape factor, S_k, is another parameter that influences how much the functional group, k, contributes to molecule properties. To indicate strong association interaction, such as hydrogen bond present in the molecules, such as H_2O, the short-ranged square-well potential is introduced to define this type of interaction. It is placed in any segment of the compound as required. The square-well potential [74] between type a, association site, on segment k and type b, association site on segment l is provided by:

$$\phi_{kl,\text{ab}}^{\text{HB}}(r_{kl,\text{ab}}) = \begin{cases} -\varepsilon_{kl,\text{ab}}^{\text{HB}} & \text{if } r_{kl,\text{ab}} \leq r_{kl,\text{ab}}^{\text{c}} \\ 0 & \text{if } r_{kl,\text{ab}} > r_{kl,\text{ab}}^{\text{c}} \end{cases} \tag{16}$$

where $\varepsilon_{kl,\text{ab}}^{\text{HB}}$ is the association energy; $r_{kl,\text{ab}}$ is the distance between sites a and b; and $r_{kl,\text{ab}}^{\text{c}}$ is the cut-off distance between sites a and b that can be expressed in terms of bonding volume, $K_{kl,\text{ab}}$. To fully characterise the associated group, the number of distinct site types, $N_{\text{ST},k}$, and the number of sites of each type, $n_{k,\text{a}}$, are also required and provided prior to simulation.

The like parameters, which characterise interactions between identical functional groups, are determined by regression to experimental data, such as vapour pressures and compress liquid densities from a series of molecules containing that group [71]. The unlike parameters, which define the interactions between different functional groups,

can be calculated using combining rules or otherwise estimated by regression against experimental data. The following set of equations gives the combining rules:

$$
\left.
\begin{aligned}
\sigma_{kl} &= \tfrac{1}{2}(\sigma_{kk} + \sigma_{ll}) \\
r_{kl} &= \tfrac{1}{2}(r_{kk} + r_{ll}) \\
\varepsilon_{kl} &= \frac{\sqrt{\sigma_{kk}^3 \sigma_{ll}^3}}{\sigma_{kl}^3}\sqrt{\varepsilon_{kk}\varepsilon_{ll}} \\
\lambda_{kl} &= 3 + \sqrt{(\lambda_{kk}-3)(\lambda_{ll}-3)} \\
\varepsilon_{kl,\mathrm{ab}}^{\mathrm{HB}} &= \sqrt{\varepsilon_{kk,\mathrm{aa}}^{\mathrm{HB}}\varepsilon_{ll,\mathrm{bb}}^{\mathrm{HB}}} \\
K_{kl,\mathrm{ab}} &= \left(\frac{\sqrt[3]{K_{kk,\mathrm{aa}}}+\sqrt[3]{K_{ll,\mathrm{bb}}}}{2}\right)^3
\end{aligned}
\right\}
\tag{17}
$$

In SAFT-γ Mie, CO_2, H_2O and N_2 are represented by a single group. The like parameters utilised for CO_2 and H_2O were found in the literature [50,73], and they are given in Table 11. However, the like parameters for nitrogen have not been developed in the literature. Therefore, in this work, we modelled nitrogen as molecular group N_2 with two fused segments, $\nu_k{}^* = 2$, and the attractive exponent is fixed to the London value, $\lambda_{kk}^a = 6$. The rest of the parameters were obtained by regression of pure nitrogen-saturated-liquid density [75] and vapour pressure data [76]. The data used to estimate group parameters include temperatures ranging from the triple point to 90 percent of the experimental critical temperature. The objective function used in the regression is as follow:

$$
f_{\mathrm{obj}} = \sum_i^N \left[\frac{p_{\exp}^{\mathrm{vap}}(T_i) - p_{\mathrm{cal}}^{\mathrm{vap}}(T_i)}{p_{\exp}^{\mathrm{vap}}(T_i)}\right]^2 + \sum_i^N \left[\frac{\rho_{\exp}^{\mathrm{sat}}(T_i) - \rho_{\mathrm{cal}}^{\mathrm{sat}}(T_i)}{\rho_{\exp}^{\mathrm{sat}}(T_i)}\right]^2
\tag{18}
$$

Table 11. Like group parameters used in SAFT-γ Mie modelling. $\nu_k{}^*$ is the number of segments constituting group S_k, the shape factor and σ_{kk} size of group k; λ_{kk}^r is the repulsive exponent; λ_{kk}^a is the attractive exponent; ε_{kk} is the Mie potential dispersion energy; $N_{\mathrm{ST},k}$ is the number of possible association site types in the group, $n_{H,k}$, $n_{e1,k}$ and $n_{e2,k}$ are the number of association sites of type H, type e_1 and e_2, respectively; and k_B is the Boltzmann constant, $k_B = 1.380648813\cdot10^{-23}$ J K^{-1}.

Group	$\nu_k{}^*$	S_k	σ_{kk}/Å	λ_{kk}^r	λ_{kk}^a	(ε_{kk}/k_B)/K	$N_{\mathrm{ST},k}$	$n_{H,k}$	$n_{e1,k}$	$n_{e2,k}$	$\varepsilon_{kk,\mathrm{He}_1}^{\mathrm{HB}}$/K	K_{kk,He_1}/ Å^3	Ref.
CO_2	2	0.8468	3.0500	26.408	5.055	207.89	2		1	1			[50]
H_2O	1	1.0000	3.0063	17.020	6.000	266.68	2	2	2		1985.4	101.69	[73]
N_2	2	0.7101	3.1779	10.1087	6.000	73.64	-	-	-	-			This work

Here, p^{vap} and ρ^{sat} denote saturated-liquid density and vapour pressure. The subscripts cal and exp are the calculated and experimental values, respectively, and N is the total number of data points. The optimised parameters are given in Table 11. The description of the saturated-liquid density and the vapour pressure of pure nitrogen obtained with the estimated parameters is shown in Figure 8. One of the features of the SAFT-γ Mie equation is the accuracy to predict second-derivative properties, such as isobaric expansivity, isothermal compressibility and heat capacity, as was demonstrated in our previous work [77–79]. Figure 9 shows the SAFT-γ Mie prediction for the isobaric heat capacity and single-phase density. The average absolute relative deviations (Δ_{AARD}) between the experimental data and the calculated data using SAFT-γ Mie modelling are summarised in Table 12. Table 12 and Figures 8 and 9 show that the SAFT-γ Mie accurately represented the vapour pressures, saturated liquid densities and single densities of pure nitrogen. It should be noted that the SAFT-γ Mie model failed to predict the heat capacity with the same accuracy as the other properties, particularly close to the critical point of nitrogen (126.19 K and 3.396 MPa) [61]. This may be because SAFT-γ Mie is an analytical equation of state and, as such, cannot faithfully describe criticality. It can be improved on the surface as a

whole but not substantially in the critical region. Table 12 also compares experimental data and calculated data using the Helmholtz energy equation of state (HEoS) for pure nitrogen implemented in REFPROP 10.0 [61]. In general, the HEoS provides a better description of the data than SAFT-γ Mie, as HEoS contains more parameters that have been fully optimised using extensive experimental data. However, SAFT-γ Mie can be considered to provide a good description of the nitrogen properties.
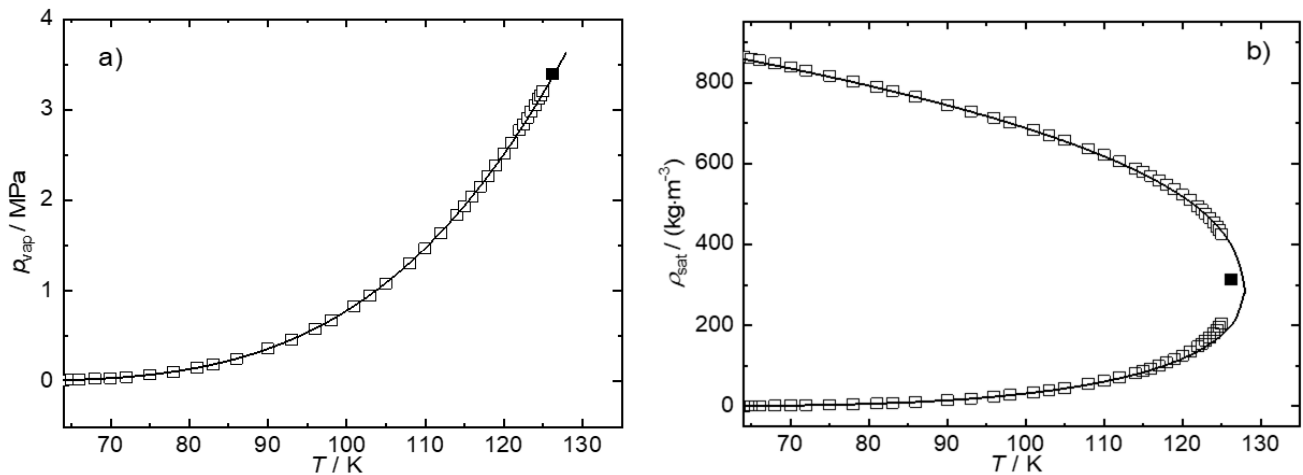
Figure 8. (**a**) Saturated densities and (**b**) vapour pressure for pure nitrogen. The empty symbols denote the experimental data [75], and the continuous line denotes the SAFT-γ Mie approach description with the parameters listed in Table 11. The filled-in black symbols represent the experimental critical point [61].
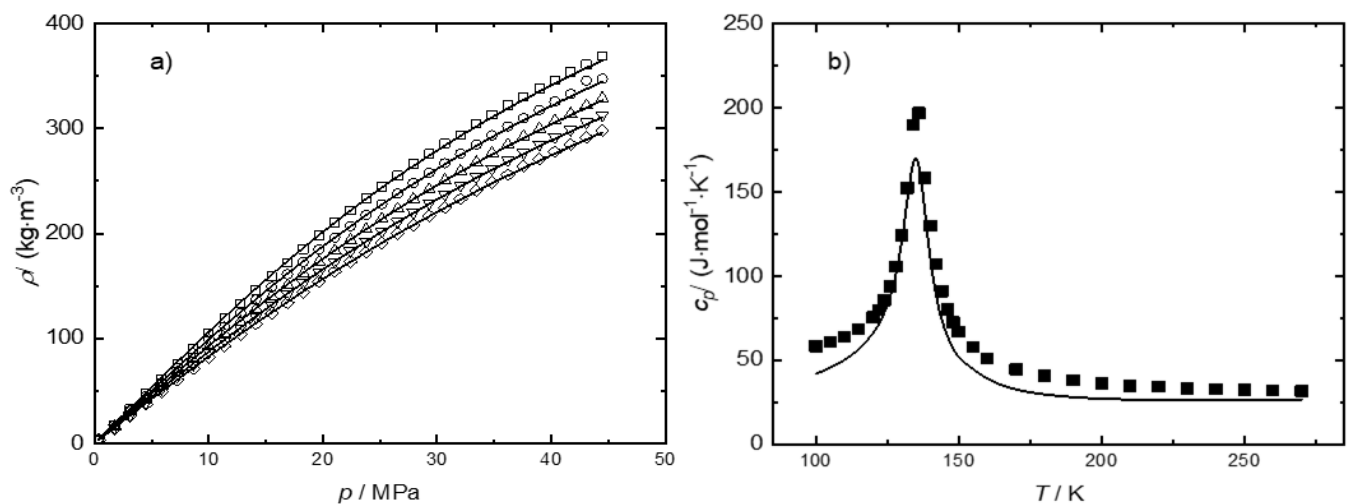
Figure 9. (**a**) Single-phase densities and (**b**) isobaric heat capacities for pure nitrogen. In (**a**), the symbols represent the experimental data [80] at temperatures of 313.15 K (squares), 333.15 K (circles), 353.15 K (triangles), 373.15 K (inverted triangles) and 393.15 (diamonds). In (**b**), the symbols represent the experimental data at 5.07 MPa [81]. The continuous lines are the predictions with the SAFT-γ Mie approach in (**a**,**b**).

Table 12. Absolute average relative deviations (Δ_{AARD}) between experimental and calculated values obtained either with the SAFT-γ Mie approach or the Helmholtz energy equation of state (Helmholtz-EoS). p_{vap}, ρ_{sat}, ρ and c_p are vapour pressure, saturated-liquid density, single-phase density and isobaric-specific heat capacity, respectively. N denotes the number of points.

Property	N	Range T/K	$10^2 \cdot \Delta_{AARD}$	$10^2 \cdot \Delta_{AARD}$	Ref
			SAFT-γ Mie	**Helmholtz-Eos**	
p_{vap}	43	64–126	0.39	0.0031	[75]
ρ_{sat}	43	64–126	0.50	0.0028	[75]
ρ	165	313–393	0.80	0.81	[80]
c_p	33	100–270	17.6	2.12	[81]

The unlike parameters of the SAFT-γ Mie approach to describe the phase behaviour of CO_2, H_2O and N_2 mixtures are given in Table 13. Only the unlike dispersion energy (ε_{kl}), the unlike association energy ($\varepsilon_{kl,He_1}^{HB}$) and the unlike association bonding volume (K_{kk,He_1}) for the (CO_2 + H_2O) system were estimated from experimental data in the literature [50]. Therefore, the unlike dispersion energy (ε_{kl}) between H_2O and N_2 required to adequately predict the water and nitrogen phase behaviour was estimated here by fitting our VLE data at 373 K, which are given in Table 13. This parameter is then used to predict other isotherms, as discussed in the next section. Furthermore, it was needed to estimate the unlike parameter between CO_2 and N_2 for the VLE prediction of the (CO_2 + H_2O + N_2) system. In this work, the unlike dispersion energy (ε_{kl}) and the repulsive exponent (λ_{kl}^r) between CO_2 and N_2 groups were determined by fitting the experimental vapour–liquid equilibrium data at 258.15 and 273.15 K, respectively [54].

Table 13. Unlike group dispersion interaction energies (ε_{kl}), repulsive exponent (λ_{kk}^r), association energy ($\varepsilon_{kl,He_1}^{HB}$) and association bonding volume (K_{kk,He_1}) used the SAFT-γ Mie Modelling, where k_B is Boltzmann's constant. CR indicates values obtained using the combining rule, Equation (17) [1].

Group, k	Group l	(ε_{kl}/k_B)/K	λ_{kk}^r	Site a of Group k	Site b of Group l	$\varepsilon_{kl,He_1}^{HB}/$	K_{kk,He_1}	Ref
CO_2	H_2O	226.38	CR	H	e	1398.1	91.419	[50]
H_2O_2	N_2	126.59	CR					This work
CO_2	N_2	151.90	20.27					This work

[1] The remaining unlike cross-interaction parameters between groups were estimated using combining rules, Equation (17).

The objective function used in the optimisation of unlike parameter is given by:

$$f_{obj} = \sum_i^N \left[\frac{p_{exp}(T_i, x_i) - p_{cal}(T_i, x_i)}{p_{exp}(T_i, x_i)} \right]^2 + \sum_i^N \left[\frac{p_{exp}(T_i, y_i) - p_{cal}(T_i, y_i)}{p_{exp}(T_i, y_i)} \right]^2 \tag{19}$$

where N is the total number of data points; $p_{exp}(T_i, x_i)$ and $p_{cal}(T_i, x_i)$ represent the experimental and calculated bubble pressures, respectively; and $p_{exp}(T_i, y_i)$ and $p_{cal}(T_i, y_i)$ are the experimental and calculated dew pressures, respectively. We used an objective function based on the bubble and dew pressures because this provided more stable convergence than using an objective function based on mole fractions. The rest of the cross-interaction parameters between unlike groups were calculated using combining rules, Equation (17).

The predictions of SAFT-γ Mie with the parameters listed in Table 13 were compared with the experimental VLE data of the (CO_2 + N_2) system for other isotherms. This was done to assess the validity of the optimised unlike parameters between the CO_2 and N_2 groups. Figure 10 shows a comparison between the SAFT-γ Mie description and experimental data. Table 14 give the absolute average deviations for the bubble and dew compositions. SAFT-γ Mie gives a good description of the bubble and dew pressure in an extensive temperature range. However, the critical points at 258 and 273 K were overpredicted. The SAFT-γ

model also captures the crossover effect of nitrogen solubility in the liquid phase at about 12 MPa. Above that pressure, the solubility increases with increased temperature, whereas the opposite occurs at lower pressure.
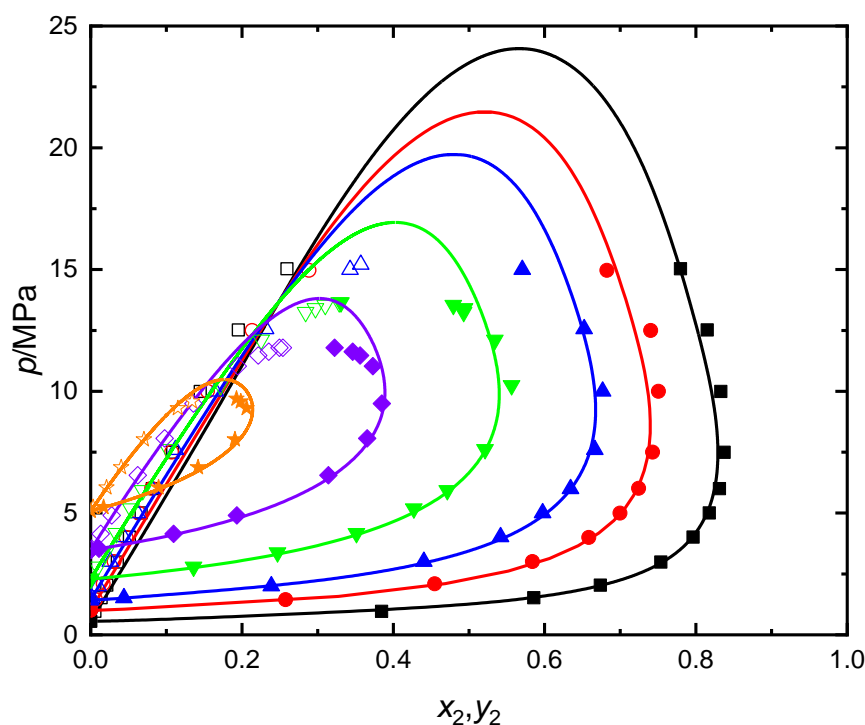
Figure 10. Vapour–liquid equilibrium for the (CO_2(1) + N_2(2)) system at temperatures of (black) 218 K, (red) 233 K, (blue) 243 K, (green) 258 K, (purple) 273 K and (orange) 288 K. The empty and filled-in symbols represent the bubble and dew point pressures, respectively, published by Fadiño et al. [54]. The continuous lines represent the description of the SAFT-γ Mie model.

Table 14. Absolute average deviation for the bubble (Δ_{AADx}) and dew compositions (Δ_{AADy}) between the SAFT-γ Mie model, the γ-φ model description and experimental data. *N* represents the number data points. For the CO_2 + H_2O + N_2 ternary system, Δ_{AADx} and Δ_{AADy} represent the CO_2 molar fraction.

System	N	Range T/K	Δ_{AADx}		Δ_{AADy}	
			SAFT-γ Mie	γ-φ Model	SAFT-γ Mie	γ-φ Model
CO_2 + N_2	68	218–288	0.017	-	0.023	-
H_2O + N_2	50	323–423	0.00014	0.00005	0.008	0.014
CO_2 + H_2O + N_2	30	323–473	0.0004	0.0006	0.011	0.013

Furthermore, the SAFT-γ Mie method with the parameters set given in Tables 12 and 13 was tested for its ability to predict the vapour–liquid equilibrium of the (CO_2 + H_2O + N_2) ternary system in the next section, as all the required group interaction parameters were obtained for the pure components and binary systems. All SAFT-γ Mie calculations were performed in gPROMS© software developed by PSE Ltd. [82] The numerical solvers supplied by gPROMS were used to minimise the objective function in the estimation of both like and unlike parameters. The starting values of the parameters and their limits were defined in the program, and the Sobol sequence [83] was used to produce a good sampling of the provided parameter space. Usually, the number of Sobol points was about 5000. The Lenvenberg–Marquardt algorithm [84,85] was used to minimise the objective function. Furthermore, a sensitive analysis of the optimised parameters is presented in the Supporting Information.

5. Discussion

Figures 4 and 5 show the phase behaviour description from γ-φ and SAFT-γ Mie models and the experimental data for the (H_2O + N_2) system. The absolute average deviations, Δ_{AADx} and Δ_{AADy}, for the bubble and dew compositions, respectively, are given in Table 14. As can be seen in Figure 4, the dew-point compositions of nitrogen were under-estimated by the γ-φ approach, with Δ_{AADy} = 0.014, whereas the SAFT-γ Mie model accurately describes these data, with Δ_{AADy} = 0.008. The solubility of nitrogen in the aqueous phase, including the solubility minimum, was excellently described by the γ-φ approach (see Figures 4 and 5). However, the SAFT-γ Mie model and the γ-φ approach were unable to predict the nitrogen solubilities, even after fitting the dispersion interaction energy parameters. Additionally, the minimum solubility of nitrogen in the aqueous phase was not captured by the SAFT-γ Mie equation. For a similar mixture (H_2O + CH_4), SAFT-γ Mie also did not capture the solubility minimum [50]. The unlike repulsive group exponent was fitted to experimental data in the SAFT-γ Mie model to examine whether the solubility predictions could be improved. Unfortunately, the improvements in the solubility were minimal, but the addition of the value of another fitted parameter reduces the model's predictive capability. Therefore, it was decided to report the model with only one determined parameter. One of the probable explanations for the γ-φ model's superior performance in describing the nitrogen solubility in water could be that the Henry constant is a polynomial function of temperature. This provides great flexibility to the model for representing solubility data, including the minimum value.

The vapour–liquid equilibrium data and the description from γ-φ and SAFT-γ Mie for the (CO_2 + H_2O + N_2) system are shown in Figures 6 and 7. Table 14 shows the absolute average deviation between the experimental data and the prediction for both models. In general, we found good agreement between experimental data and predictions from both models. Table 14 shows that the absolute average deviation was similar for the two models. The improvement in the solubility predictions of SAFT-γ Mie for the ternary system with respect to the (H_2O + N_2) binary system might be related to the SAFT-γ Mie providing a better description of the (CO_2 + H_2O) binary system [50]. In the γ-φ model for the (CO_2 + H_2O + N_2) system, it should be noted that activity coefficients of CO_2 were confined to a narrow range between 0.90 to 1.20 because CO_2 solubility was very low in the aqueous phase. This contrasts with the CO_2 activity coefficients in the binary CO_2 + H_2O system, which deviated much more from unity [46] because the CO_2 solubility in the binary system is about twice that in the ternary at the same temperature and pressure. Therefore, the liquid phase in the ternary system with a mole ratio of 1 between CO_2 and N_2 behaves closer to an ideal solution compared to the (CO_2 + H_2O) binary system.

Figure 11 compares the calculated vapour–liquid equilibria for the (CO_2 + H_2O + N_2) ternary system and the two binary subsystems: (H_2O + N_2) and (CO_2 + H_2O) at two temperatures. It can be seen in Figure 11 that the gas solubility in the aqueous phase for the ternary mixture was in between the solubilities of the respective binary subsystems for both temperatures. On the contrary, the vapour-phase behaviour of the ternary system is closer to that of the (H_2O + N_2) mixture than the CO_2 + H_2O system. At 323 K, the minimum water concentration in the vapour phase found in the CO_2 + H_2O system vanished in the ternary system. This is might be another indication of the ideal behaviour of the ternary mixture.
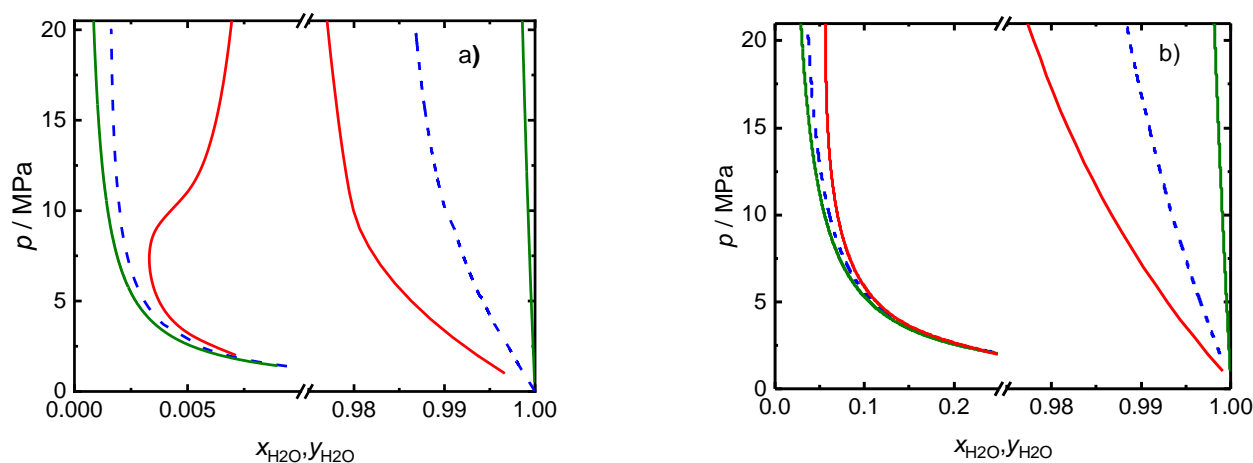
Figure 11. Calculated vapor–liquid equilibrium (VLE) for (N_2 + H_2O) (green continue line), (CO_2 + N_2 + H_2O) (blue dash line) and (CO_2 + H_2O) (red continue line) at 323 K (**a**) and 423 K (**b**). VLE for the CO_2 + H_2O system calculated with the model proposed by Spycher et al. [20,21]. The VLE for the (CO_2 + N_2 + H_2O) system and the dew points of (N_2 + H_2O) was calculated by the SAFT-γ Mie model with parameters from Tables 11 and 13. The bubble points for (N_2 + H_2O) were calculated with the γ-φ model [46].

6. Conclusions

New vapour–liquid equilibrium data were reported for a binary (N_2 + H_2O) system and a (CO_2 + N_2 + H_2O) ternary system at pressures of 1 to 20 MPa and temperatures of 323.15 to 473.15 K. The mole ratio between the CO_2 and N_2 fed in the ternary system was fixed to a value of unity. The experimental data were compared with calculations based on SAFT-γ Mie and γ-φ models. The SAFT-γ Mie model described the water concentration in the vapour phase for the binary system better than the γ-φ model, whereas the γ-φ model was superior in calculating nitrogen solubility in the water phase, including the minimum of solubility. The optimisation of other unlike parameters, such as lambda repulsive, did not significantly improve the solubility prediction of the SAFT-γ Mie model. Both SAFT-γ Mie and γ-φ approaches provided a good description of the vapour composition of the (CO_2 + N_2 + H_2O) ternary system under the conditions studied in this paper. Therefore, either of the models could be used to predict the ternary system on other isotherms. However, we recommend that the phase behaviour for the (N_2 + H_2O) binary system be calculated by the γ-φ models.

References

1. *Special Report on Global Warming of 1.5 °C*; Intergovernmental Panel on Climate Change: Incheon, Korea, 2018.
2. Yan, Y.; Manovic, V.; Anthony, E.J.; Clough, P.T. Techno-economic analysis of low-carbon hydrogen production by sorption enhanced steam methane reforming (SE-SMR) processes. *Energy Convers. Manag.* **2020**, *226*, 113530. [CrossRef]
3. Bui, M.; Adjiman, C.S.; Bardow, A.; Anthony, E.J.; Boston, A.; Brown, S.; Fennell, P.S.; Fuss, S.; Galindo, A.; Hackett, L.A.; et al. Carbon capture and storage (CCS): The way forward. *Energy Environ. Sci.* **2018**, *11*, 1062–1176. [CrossRef]
4. Abbas, Z.; Mezher, T.; Abu-Zahra, M.R.M. CO_2 purification. Part I: Purification requirement review and the selection of impurities deep removal technologies. *Int. J. Greenh. Gas Control* **2013**, *16*, 324–334. [CrossRef]
5. *ISO/TR 27921:2020*; Carbon Dioxide Capture, Transportation, and Geological Storage—Cross Cutting Issues—CO_2 Stream Composition. ISO: Geneva, Switzerland, 2020; p. 45.
6. Tenorio, M.-J.; Parrott, A.J.; Calladine, J.A.; Sanchez-Vicente, Y.; Cresswell, A.J.; Graham, R.S.; Drage, T.C.; Poliakoff, M.; Ke, J.; George, M.W. Measurement of the vapour–liquid equilibrium of binary and ternary mixtures of CO_2, N_2 and H_2, systems which are of relevance to CCS technology. *Int. J. Greenh. Gas Control* **2015**, *41*, 68–81. [CrossRef]
7. Souza, L.F.S.; Al Ghafri, S.Z.S.; Trusler, J.P.M. Measurement and modelling of the vapor–liquid equilibrium of (CO_2 + CO) at temperatures between (218.15 and 302.93) K at pressures up to 15 MPa. *J. Chem. Thermodyn.* **2018**, *126*, 63–73. [CrossRef]
8. Efika, E.C.; Hoballah, R.; Li, X.; May, E.F.; Nania, M.; Sanchez-Vicente, Y.; Martin Trusler, J.P. Saturated phase densities of (CO_2+H_2O) at temperatures from (293 to 450) K and pressures up to 64 MPa. *J. Chem. Thermodyn.* **2016**, *93*, 347–359. [CrossRef]
9. Tan, Y.; Nookuea, W.; Li, H.; Thorin, E.; Yan, J. Property impacts on Carbon Capture and Storage (CCS) processes: A review. *Energy Convers. Manag.* **2016**, *118*, 204–222. [CrossRef]
10. Trusler, J.P.M. Thermophysical Properties and Phase Behavior of Fluids for Application in Carbon Capture and Storage Processes. *Annu. Rev. Chem. Biomol. Eng.* **2017**, *8*, 381–402. [CrossRef]
11. Battino, R.; IUPAC. *Nitrogen and Air. Solubility Data Series*; Pergamon Press: Oxford, UK, 1982; pp. 1–565.
12. Smith, N.O.; Kelemen, S.; Nagy, B. Solubility of natural gases in aqueous salt solutions—II: Nitrogen in aqueous NaCl, $CaCl_2$, Na_2SO_4 and $MgSO_4$ at room temperatures and at pressures below 1000 psia. *Geochim. Cosmochim. Acta* **1962**, *26*, 921–926. [CrossRef]
13. O'Sullivan, T.D.; smith, N.O.; Nagy, B. Solubility of natural gases in aqueous salt solutions—III Nitrogen in aqueous NaCl at high pressures. *Geochim. Cosmochim. Acta* **1966**, *30*, 617–619. [CrossRef]
14. Wiebe, R.; Gaddy, V.L.; Heinss, C. Solubility of Nitrogen in Water in 250 °C from 25 to 1000 Atmospheres. *Ind. Eng. Chem.* **1932**, *24*, 927. [CrossRef]
15. Wiebe, R.; Gaddy, V.L.; Heins, C. The Solubility of Nitrogen in Water at 50, 75 and 100° C from 25 to 1000 Atmospheres. *J. Am. Chem. Soc.* **1933**, *55*, 947–953. [CrossRef]
16. Folas, G.K.; Froyna, E.W.; Lovland, J.; Kontogeorgis, G.M.; Solbraa, E. Data and prediction of water content of high pressure nitrogen, methane and natural gas. *Fluid Phase Equilibria* **2007**, *252*, 162–174. [CrossRef]
17. Mohammadi, A.H.; Chapoy, A.; Tohidi, B.; Richon, D. Water Content Measurement and Modeling in the Nitrogen + Water System. *J. Chem. Eng. Data* **2005**, *50*, 541–545. [CrossRef]
18. Rigby, M.; Prausnitz, J.M. Solubility of water in compressed nitrogen, argon, and methane. *J. Phys. Chem.* **1968**, *72*, 330–334. [CrossRef]
19. Maslennikova, V.Y.; Vdovina, N.A.; Tsiklis, D.S. Solubility of Water in Compressed Nitrogen. *Russ. J. Phys. Chem.* **1971**, *45*, 1354.
20. Spycher, N.; Pruess, K.; Ennis-King, J. CO_2-H_2O mixtures in the geological sequestration of CO_2. I. Assessment and calculation of mutual solubilities from 12 to 100 °C and up to 600 bar. *Geochim. Cosmochim. Acta* **2003**, *67*, 3015–3031. [CrossRef]
21. Spycher, N.; Pruess, K. A Phase-Partitioning Model for CO_2–Brine Mixtures at Elevated Temperatures and Pressures: Application to CO_2-Enhanced Geothermal Systems. *Transp. Porous Media* **2010**, *82*, 173–196. [CrossRef]
22. Diamond, L.W.; Akinfiev, N.N. Solubility of CO_2 in water from −1.5 to 100 °C and from 0.1 to 100 MPa: Evaluation of literature data and thermodynamic modelling. *Fluid Phase Equilibria* **2003**, *208*, 265–290. [CrossRef]
23. Chapoy, A.; Mohammadi, A.H.; Chareton, A.; Tohidi, B.; Richon, D. Measurement and Modeling of Gas Solubility and Literature Review of the Properties for the Carbon Dioxide−Water System. *Ind. Eng. Chem. Res.* **2004**, *43*, 1794–1802. [CrossRef]
24. Goodman, J.B.; Krase, N.W. Solubility of Nitrogen in Water at High Pressures and Temperatures. *Ind. Eng. Chem.* **1931**, *23*, 401–404. [CrossRef]
25. Saddington, A.W.; Krase, N.W. Vapor—Liquid Equilibria in the System Nitrogen—Water. *J. Am. Chem. Soc.* **1934**, *56*, 353–361. [CrossRef]

26. Sidorov, I.P.; Kazarnovskii, Y.S.; Goldman, A.M. The Solubility of Water in compressed Gases. *Tr. Gos. Nauchno Issled. Proektn. Inst. Azotn. Promst. Prod. Org. Sin.* **1953**, *1*, 48–67.

27. Bukacek, R.F. Equilibrium Moisture Content of Natural Gases. *Inst. Gas Technol. Chikago Res. Bull.* **1955**, *8*, 1–19.

28. Maslennikova, V.Y. Solubility of Nitrogen in Water. *Tr. Gos. Nauchno Issled. Proektn. Inst. Azotn. Promst. Prod. Org. Sin.* **1971**, *12*, 82–87.

29. Kosyakov, N.E.; Ivchenko, B.I.; Krishtopa, P.P. Moisture Contents of Compressed Nitrogen and Hydrogen at Low Temperatures. *J. Appl. Chem. USSR* **1977**, *50*, 2436–2438.

30. Brunner, G. *Phase Equilibria in Presence of Compressed Gases and Their Relevance to the Separation of Low-Volatile Substances*; University Erlangen-Nuernberg: Erlangen, Germany, 1978.

31. Gillespie, P.C.; Wilson, G.M. Vapor-Liquid Equilibrium Data on Water-Substitute Gas Components: $N_2 + H_2O$, $H_2 + H_2O$, CO + H_2O, $H_2 + CO + H_2O$, and $H_2S + H_2O$. *GPA Res. Rep.* **1980**, 1–34. [CrossRef]

32. Japas, M.L.; Franck, E.U. High Pressure Phase Equilibria and PVT-Data. of the Water-Nitrogen System to 673 K and 250 MPa. *Ber. Der Bunsenges. FÜR Phys. Chem.* **1985**, *89*, 793–800. [CrossRef]

33. Li, Y.-K.; Nghiem, L.X. Phase equilibria of oil, gas and water/brine mixtures from a cubic equation of state and henry's law. *Can. J. Chem. Eng.* **1986**, *64*, 486–496. [CrossRef]

34. Alvarez, J.; Fernández-Prini, R. A semiempirical procedure to describe the thermodynamics of dissolution of non-polar gases in water. *Fluid Phase Equilibria* **1991**, *66*, 309–326. [CrossRef]

35. Fenghour, A.; Wakeham, W.A.; Ferguson, D.; Scott, A.C.; Watson, J.T.R. Densities of (water + nitrogen) in the temperature range 533 K to 703 K and at pressures up to 31 MPa. *J. Chem. Thermodyn.* **1993**, *25*, 1151–1159. [CrossRef]

36. Ugrozov, V.V. Equilibrium Compositions of Vapor-Gas Mixtures over Solutions. *Russ. J. Phys. Chem.* **1996**, *70*, 1240–1241.

37. Blanco, S.A.T.; Velasco, I.; Rauzy, E.; Otín, S. Water dew points of binary nitrogen+water and propane + water mixtures. Measurement and correlation. *Fluid Phase Equilibria* **1999**, *161*, 107–117. [CrossRef]

38. Blanco, S.T.; Velasco, I.; Otin, S. Dew Points of Binary Nitrogen + Water Mixtures. *Phys. Chem. Liq.* **2002**, *40*, 167–172. [CrossRef]

39. Chapoy, A.; Mohammadi, A.H.; Tohidi, B.; Richon, D. Gas Solubility Measurement and Modeling for the Nitrogen + Water System from 274.18 K to 363.02 K. *J. Chem. Eng. Data* **2004**, *49*, 1110–1115. [CrossRef]

40. Tabasinejad, F.; Moore, R.G.; Mehta, S.A.; Van Fraassen, K.C.; Barzin, Y.; Rushing, J.A.; Newsham, K.E. Water Solubility in Supercritical Methane, Nitrogen, and Carbon Dioxide: Measurement and Modeling from 422 to 483 K and Pressures from 3.6 to 134 MPa. *Ind. Eng. Chem. Res.* **2011**, *50*, 4029–4041. [CrossRef]

41. Liu, Y.; Hou, M.; Ning, H.; Yang, D.; Yang, G.; Han, B. Phase Equilibria of $CO_2 + N_2 + H_2O$ and $N_2 + CO_2 + H_2O + NaCl + KCl + CaCl_2$ Systems at Different Temperatures and Pressures. *J. Chem. Eng. Data* **2012**, *57*, 1928–1932. [CrossRef]

42. Muromachi, S.; Miyamoto, H.; Ohmura, R. Solubility of Nitrogen Gas in Aqueous Solution of Tetra-n-Butylammonium Bromide. *Int. J. Thermophys.* **2017**, *38*, 173. [CrossRef]

43. Zelvenskii, Y.D. Solubility of the Gas-Mixtures $CO_2 + N_2$ and $CO_2 + H_2$ in Water under Pressure. *Zh. Prikl. Khim.* **1939**, *12*, 1312–1329.

44. Foltran, S.; Vosper, M.E.; Suleiman, N.B.; Wriglesworth, A.; Ke, J.; Drage, T.C.; Poliakoff, M.; George, M.W. Understanding the solubility of water in carbon capture and storage mixtures: An FTIR spectroscopic study of $H_2O + CO_2 + N_2$ ternary mixtures. *Int. J. Greenh. Gas Control* **2015**, *35*, 131–137. [CrossRef]

45. Hassanpouryouzband, A.; Farahani, M.V.; Yang, J.; Tohidi, B.; Chuvilin, E.; Istomin, V.; Bukhanov, B. Solubility of Flue Gas or Carbon Dioxide-Nitrogen Gas Mixtures in Water and Aqueous Solutions of Salts: Experimental Measurement and Thermodynamic Modeling. *Ind. Eng. Chem. Res.* **2019**, *58*, 3377–3394. [CrossRef]

46. Hou, S.-X.; Maitland, G.C.; Trusler, J.P.M. Measurement and modeling of the phase behavior of the (carbon dioxide+water) mixture at temperatures from 298.15 K to 448.15 K. *J. Supercrit. Fluids* **2013**, *73*, 87–96. [CrossRef]

47. Perez, R.J.; Heidemann, R.A. Coupling an equation of state and Henry's Law to model the phase equilibria of gases and brines: Examples in the N_2–H_2O–NaCl system. *J. Geochem. Explor.* **2006**, *89*, 331–334. [CrossRef]

48. Kontogeorgis, G.M.; Michelsen, M.L.; Folas, G.K.; Derawi, S.; von Solms, N.; Stenby, E.H. Ten Years with the CPA (Cubic-Plus-Association) Equation of State. Part 2. Cross-Associating and Multicomponent Systems. *Ind. Eng. Chem. Res.* **2006**, *45*, 4869–4878. [CrossRef]

49. dos Ramos, M.C.; Blas, F.J.; Galindo, A. Phase Equilibria, Excess Properties, and Henry's Constants of the Water + Carbon Dioxide Binary Mixture. *J. Phys. Chem. C* **2007**, *111*, 15924–15934. [CrossRef]

50. Papaioannou, V.; Calado, F.; Lafitte, T.; Dufal, S.; Sadeqzadeh, M.; Jackson, G.; Adjiman, C.S.; Galindo, A. Application of the SAFT-γ Mie group contribution equation of state to fluids of relevance to the oil and gas industry. *Fluid Phase Equilibria* **2016**, *416*, 104–119. [CrossRef]

51. Kunz, O.; Wagner, W. The GERG-2008 Wide-Range Equation of State for Natural Gases and Other Mixtures: An Expansion of GERG-2004. *J. Chem. Eng. Data* **2012**, *57*, 3032–3091. [CrossRef]

52. Gernert, J.; Span, R. Accurate property models for application in CCS processes. In Proceedings of the Asian Thermophysical Properties Conference, Beijing, China, 19–22 October 2010; pp. 1832–1842.

53. Gernert, J.; Span, R. EOS–CG: A Helmholtz energy mixture model for humid gases and CCS mixtures. *J. Chem. Thermodyn.* **2016**, *93*, 274–293. [CrossRef]

54. Fandiño, O.; Trusler, J.P.M.; Vega-Maza, D. Phase behavior of (CO_2 + H_2) and (CO_2 + N_2) at temperatures between (218.15 and 303.15) K at pressures up to 15 MPa. *Int. J. Greenh. Gas Control* **2015**, *36*, 78–92. [CrossRef]

55. Wentworth, W.E.; Vasnin, S.V.; Stearns, S.D.; Meyer, C.J. Pulsed discharge helium ionization detector. *Chromatographia* **1992**, *34*, 219–225. [CrossRef]

56. McNair, H.M.; Miller, J.M. *Basic Gas Chromatography*; Wiley: Hoboken, NJ, USA, 2009.

57. JCGM, J. Evaluation of measurement data—Guide to the expression of uncertainty in measurement. *Int. Organ. Stand. Geneva ISBN* **2008**, *50*, 134.

58. Spycher, N.; Pruess, K. CO_2-H_2O mixtures in the geological sequestration of CO_2. II. Partitioning in chloride brines at 12–100 °C and up to 600 bar. *Geochim. Cosmochim. Acta* **2005**, *69*, 3309–3320. [CrossRef]

59. Ou, W.; Geng, L.; Lu, W.; Guo, H.; Qu, K.; Mao, P. Quantitative Raman spectroscopic investigation of geo-fluids high-pressure phase equilibria: Part II. Accurate determination of CH_4 solubility in water from 273 to 603 K and from 5 to 140 MPa and refining the parameters of the thermodynamic model. *Fluid Phase Equilibria* **2015**, *391*, 18–30. [CrossRef]

60. Van Konynenburg, P.; Scott, R. Critical lines and phase equilibria in binary van der Waals mixtures. *Philos. Trans. R. Soc. London. Ser. A Math. Phys. Sci.* **1980**, *298*, 495–540.

61. Lemmon, E.W.; Bell, I.H.; Huber, M.L.; McLinden, M.O. *NIST Standard Reference Database 23: Reference Fluid Thermodynamic and Transport Properties-REFPROP, version 10.0*; Standard Reference Data Program; National Institute of Standards and Technology: Gaithersburg, MD, USA, 2018. [CrossRef]

62. Aparicio-Martínez, S.; Hall, K.R. Phase equilibria in water containing binary systems from molecular based equations of state. *Fluid Phase Equilibria* **2007**, *254*, 112–125. [CrossRef]

63. Schouten, J.; van Hinsberg, M.; Scheerboom, M.; Michels, J. Peculiarities in the high-pressure phase behaviour of binary mixtures of nitrogen with methane, helium and water. *J. Phys. Condens. Matter* **1999**, *6*, A187. [CrossRef]

64. Mao, S.; Duan, Z. A thermodynamic model for calculating nitrogen solubility, gas phase composition and density of the N2–$H2O$–NaCl system. *Fluid Phase Equilibria* **2006**, *248*, 103–114. [CrossRef]

65. Sedlbauer, J.; O'Connell, J.P.; Wood, R.H. A new equation of state for correlation and prediction of standard molal thermodynamic properties of aqueous species at high temperatures and pressures. *Chem. Geol.* **2000**, *163*, 43–63. [CrossRef]

66. Fernández-Prini, R.; Alvarez, J.L.; Harvey, A.H. Henry's Constants and Vapor–Liquid Distribution Constants for Gaseous Solutes in H_2O and D_2O at High Temperatures. *J. Phys. Chem. Ref. Data* **2003**, *32*, 903–916. [CrossRef]

67. Renon, H.; Prausnitz, J.M. Local compositions in thermodynamic excess functions for liquid mixtures. *AIChE J.* **1968**, *14*, 135–144. [CrossRef]

68. Abudour, A.; Mohammad, S.; Gasem, K. Modeling high-pressure phase equilibria of coalbed gases/water mixtures with the Peng-Robinson equation of state. *Fluid Phase Equilibria* **2012**, *319*, 77–89. [CrossRef]

69. Mantovani, M.; Chiesa, P.; Valenti, G.; Gatti, M.; Consonni, S. Supercritical pressure–density–temperature measurements on CO_2–N_2, CO_2–O_2 and CO_2–Ar binary mixtures. *J. Supercrit. Fluids* **2012**, *61*, 34–43. [CrossRef]

70. Chow, Y.T.F.; Maitland, G.C.; Trusler, J.P.M. Interfacial tensions of the (CO_2 + N_2 + H_2O) system at temperatures of (298 to 448) K and pressures up to 40 MPa. *J. Chem. Thermodyn.* **2016**, *93*, 392–403. [CrossRef]

71. Papaioannou, V.; Lafitte, T.; Avendano, C.; Adjiman, C.S.; Jackson, G.; Muller, E.A.; Galindo, A. Group contribution methodology based on the statistical associating fluid theory for heteronuclear molecules formed from Mie segments. *J. Chem. Phys.* **2014**, *140*, 054107. [CrossRef]

72. Dufal, S.; Papaioannou, V.; Sadeqzadeh, M.; Pogiatzis, T.; Chremos, A.; Adjiman, C.S.; Jackson, G.; Galindo, A. Prediction of Thermodynamic Properties and Phase Behavior of Fluids and Mixtures with the SAFT-gamma Mie Group-Contribution Equation of State. *J. Chem. Eng. Data* **2014**, *59*, 3272–3288. [CrossRef]

73. Dufal, S.; Lafitte, T.; Haslam, A.J.; Galindo, A.; Clark, G.N.I.; Vega, C.; Jackson, G. The A in SAFT: Developing the contribution of association to the Helmholtz free energy within a Wertheim TPT1 treatment of generic Mie fluids. *Mol. Phys.* **2015**, *113*, 948–984. [CrossRef]

74. Haslam, A.J.; Gonzalez-Perez, A.; Di Lecce, S.; Khalit, S.H.; Perdomo, F.A.; Kournopoulos, S.; Kohns, M.; Lindeboom, T.; Wehbe, M.; Febra, S.; et al. Expanding the Applications of the SAFT-gamma Mie Group-Contribution Equation of State: Prediction of Thermodynamic Properties and Phase Behavior of Mixtures. *J. Chem. Eng. Data* **2020**, *65*, 5862–5890. [CrossRef]

75. Nowak, P.; Kleinrahm, R.; Wagner, W. Measurement and Correlation of the (P, ρ, T) Relation of Nitrogen I. The Homogeneous Gas and Liquid Regions in the Temperature Range from 66 K to 340 K at Pressures up to 12 MPa. *J. Chem. Thermodyn. J. Chem. Thermodyn.* **1997**, *29*, 1137–1156. [CrossRef]

76. Wagner, W. New vapour pressure measurements for argon and nitrogen and a new method for establishing rational vapour pressure equations. *Cryogenics* **1973**, *13*, 470–482. [CrossRef]

77. Sanchez-Vicente, Y.; Tay, W.J.; Al Ghafri, S.Z.; Trusler, J.P.M. Thermodynamics of carbon dioxide-hydrocarbon systems. *Appl. Energy* **2018**, *220*, 629–642. [CrossRef]

78. Sanchez-Vicente, Y.; Tay, W.J.; Al Ghafri, S.Z.; Efika, E.C.; Trusler, J.P.M. Density and Phase Behavior of the CO_2 + Methylbenzene System in Wide Ranges of Temperatures and Pressures. *Ind. Eng. Chem. Res.* **2020**, *59*, 7224–7237. [CrossRef]

79. Sanchez-Vicente, Y.; Trusler, J.P.M. Saturated-Phase Densities of (CO_2 + Methylcyclohexane) at Temperatures from 298 to 448 K and Pressures up to the Critical Pressure. *J. Chem. Eng. Data* **2022**, *67*, 54–66. [CrossRef]

80. Zolghadr, A.; Riazi, M.; Escrochi, M.; Ayatollahi, S. Investigating the Effects of Temperature, Pressure, and Paraffin Groups on the N$_2$ Miscibility in Hydrocarbon Liquids using the Interfacial Tension Measurement Method. *Ind. Eng. Chem. Res.* **2013**, *52*, 9851–9857. [CrossRef]

81. van Kasteren, P.H.G.; Zeldenrust, H. A Flow Calorimeter for Condensable Gases at Low Temperatures and High Pressures. 2. Compilation of Experimental Results and Comparison with Predictions Based on a Modified Redlich-Kwong Equation of State. *Ind. Eng. Chem. Fundam.* **1979**, *18*, 339–345. [CrossRef]

82. PSE Ltd. gPROMS V.7.0.7. 2021. Available online: http://www.psenterprise.com (accessed on 10 April 2022).

83. Sobol, I.M. On the distribution of points in a cube and the approximate evaluation of integrals. *USSR Comput. Math. Math. Phys.* **1967**, *7*, 86–112. [CrossRef]

84. Levenberg, K. A method for the solution of certain non-linear problems in least squares. *Q. Appl. Math.* **1944**, *2*, 164–168. [CrossRef]

85. Marquardt, D.W. An algorithm for least-squares estimation of nonlinear parameters. *J. Soc. Ind. Appl. Math.* **1963**, *11*, 431–441. [CrossRef]